Contrib Mineral Petrol (2011) 162:751–772
DOI 10.1007/s00410-011-0623-6

ORIGINAL PAPER

Magma storage and ascent during the 1995 eruption of Fogo, Cape Verde Archipelago

Elliot Hildner · Andreas Klügel · Folkmar Hauff

Received: 24 November 2010 / Accepted: 28 February 2011 / Published online: 16 March 2011

Abstract The 1995 eruption of Fogo (Cape Verde Islands) differed from previous eruptions by the occurrence of evolved lavas, the SW-orientation of vents, and pre-eruptive seismicity between Fogo and the adjacent (~20 km) island of Brava. We have conducted a thermobarometric and chemical study of this eruption in order to reconstruct its magma plumbing system and to test for possible connections to Brava. The bimodal eruption produced basanites (5.2–6.7 wt% MgO) and phonotephrites (2.4–2.8 wt% MgO) that are related by fractional crystallization. Clinopyroxene-melt-barometry of phenocrysts yields pressure ranges of 460–680 MPa for the basanites and 460–520 MPa for the phonotephrites. Microthermometry of CO_2-dominated fluid inclusions in olivine and clinopyroxene phenocrysts yields systematically lower pressure ranges of 200–310 MPa for basanites and 270–470 MPa for phonotephrites. The combined data indicate pre-eruptive storage of the 1995 magmas within the lithospheric mantle between 16 and 24 km depth. During eruption, the ascending magmas stalled temporarily at 8–11 km depth, within the lower crust, before they ascended to the surface in a few hours as indicated by zonations of olivine phenocrysts. Our data provide no evidence for magma storage at shallow levels (<200 MPa) or lateral magma movements beneath the Fogo-Brava platform. Sr–Nd–Pb isotope ratios of samples from Brava differ significantly from those of the 1995 and older Fogo lavas, which rules out contamination of the 1995 magmas by Brava material and indicates different mantle sources and magma plumbing systems for both islands.

Keywords Fogo · Cape Verde · Thermobarometry · Fluid inclusions · Pb–Sr–Nd isotopes

Communicated by J. Hoefs.

Electronic supplementary material The online version of this article (doi:10.1007/s00410-011-0623-6) contains supplementary material, which is available to authorized users.

E. Hildner (✉) · A. Klügel
Universität Bremen, Fachbereich Geowissenschaften,
Postfach 330440, 28334 Bremen, Germany
e-mail: hildner@uni-bremen.de

F. Hauff
IFM-GEOMAR, Leibniz Institute of Marine Sciences,
Research Divison 4, Wischhofstr. 1-3, 24148 Kiel, Germany

Introduction

Storage depths and migration paths of magmas have strong control on the evolution of magmatic systems and the dynamics of volcanic eruptions. Our understanding of pre-eruptive magmatic processes therefore critically relies on knowledge about the plumbing systems. Besides geophysical methods, petrological investigation of erupted products is the main approach that can give insight into processes occurring in the Earth's mantle and crust. The combination of petrological with geophysical data, where possible, is particularly rewarding (e.g. Peccerillo et al. 2006). For intra-plate volcanic islands, the largest volcanoes on Earth, a number of petrological studies have focused on magma storage and migration from mantle to surface (e.g. Garcia et al. 1989; Putirka 1997; Hansteen et al. 1998; Chatterjee et al. 2005; Klügel et al. 2000; Schwarz et al. 2004; Galipp et al. 2006; Stroncik et al. 2009). For the Cape Verde Archipelago, such studies have not been carried out so far, and geobarometric data are sparse (Munhá et al. 1997; Barker et al. 2009).

Fogo and the adjacent smaller island of Brava are situated on the Fogo-Brava platform at the southwestern end of the Cape Verde Archipelago (Fig. 1). Fogo is one of the world's most active volcanoes with about 30 eruptions since ~1500 AD, the last occurring in 1995 (Torres et al. 1997). Remarkably, even though Fogo is the only Cape Verde Island with historic volcanic activity, Brava is more active seismically. Most of the recent seismic activity on the archipelago occurs below the shallow channel between both islands and at Cadamosto seamount southwest of Brava (Fig. 1; Heleno 2003; Helffrich et al. 2006; Grevemeyer et al. 2010). These observations, and the discovery of numerous small volcanic cones between Cadamosto and Brava, and between Fogo and Brava, led Grevemeyer et al. (2010) to postulate two magma plumbing systems in this region, one feeding Fogo and the volcanic cones between Fogo and Brava, and another one feeding the Cadamosto seamount. The investigation of a possible connection between Fogo and Brava is a main focus of our study.

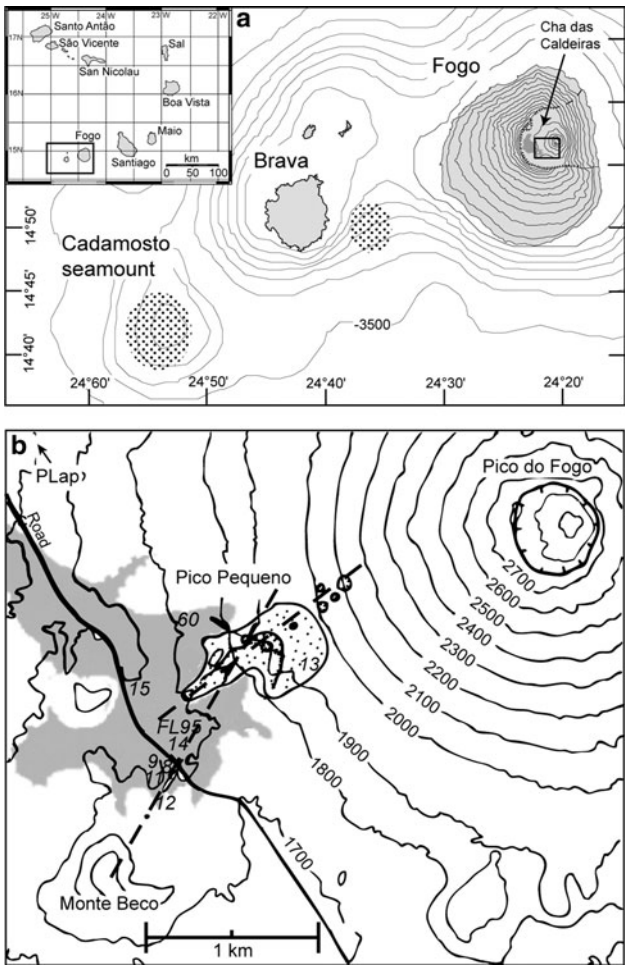

Fig. 1 **a** Location and overview map of the Cape Verde Islands (inset) and map of the Fogo-Brava platform with 500 m bathymetric contours and 200 m topographic contours on Fogo. *Dotted* areas mark seismically active regions in the channel between Fogo and Brava (seismic crisis 1994) and at Cadamosto seamount (Heleno da Silva et al. 1999; Grevemeyer et al. 2010). The rectangle shows the position of Fig. 1b. **b** Map of eruption centers and main fissures of the 1995 eruption showing the syn-eruptive scoria cone of Pico Pequeno and sample localities with numbers (modified after Brum da Silveira et al. 1997). *Gray shading* 1995 lava flows, *dotted* scoria cones

The 1995 eruption on Fogo is of particular interest for a detailed study on magma plumbing because it is well documented by eyewitness accounts, and seismic data were recorded before, during, and after the eruption (summarized in Réffega et al. 1997). On the basis of satellite-derived interferograms, Amelung and Day (2002) argued that ground deformation during the 1995 eruption resulted from a feeder dike but not from a shallow magma chamber and suggested that magma rose from a reservoir at >16.5 km depth. In contrast, Munhá et al. (1997) inferred a magma reservoir at 13 ± 3 km depth based on thermodynamic modeling using mineral compositions from ultramafic Fogo xenoliths. The 1995 eruption also shows the following peculiarities: (1) The main eruptive fissure of 1995 was oriented WSW-ENE, toward Brava island, in contrast to most other historic eruptions since 1785 where fissures were oriented roughly N–S (Day et al. 1999, Fig. 1). (2) The eruption was mineralogically and chemically zoned and produced phonotephrites, which are more evolved than other historic lavas (Munhá et al. 1997). This may be reminiscent of Brava, where phonolite rather than basalt is the most abundant recent rock type (Wolff and Turbeville 1985). (3) Seismic observations in January 1994 gave evidence for magma movements under the channel between Fogo and Brava, at depths of probably 2–7 km (Heleno da Silva et al. 1997) that could be related to the 1995 eruption.

Because of these observations, Heleno (2003) suggested a possible connection between the magma plumbing systems of Fogo and Brava and proposed that the evolved 1995 magmas could have been contaminated by Brava phonolites. This scenario would require lateral magma movement beneath the Fogo-Brava platform, as has been proposed for other localities such as Hawaii (Rhodes et al. 1989) and Galápagos (Geist et al. 1999) based on geochemical and petrological data. Alternatively, the unusual fissure orientation and the more evolved character of the 1995 lavas and the seismic crisis in 1994 near Brava could be coincidental.

In order to shed more light on Fogo's magma plumbing system, we have carried out a detailed petrological and geochemical study of the 1995 eruption with a focus on geobarometry. The main goals of our study are (1) to determine the depths of storage of the 1995 magmas; (2) to reconstruct magma pathways and ascent dynamics of the eruption; and (3) to test the hypothesis that magma migrated between Brava and Fogo during the eruption. The results improve our understanding of Fogo's recent magma

plumbing system and therefore support the ongoing monitoring activities of this potentially hazardous volcano.

Geological setting

The Cape Verde Archipelago, located in the North Atlantic ~500–800 km west of the African coast, consists of nine major islands and several small islets forming the top of the Cape Verde Swell (Fig. 1a). All islands are of volcanic origin, related to the Cape Verde mantle plume, with broadly decreasing age progression from E to W along a northern and a southern chain (summarized in Holm et al. 2008). Magmatism involves dominantly silica-undersaturated melts with basanites-tephrites and nephelinites as the most important lithologies, but phonolites and/or carbonatites also occur on several islands.

Geology of Fogo

Fogo has a diameter of ~25 km and reaches a maximum height of 2,829 m above sea level at Pico do Fogo. According to Day et al. (1999) and Foeken et al. (2009), the evolution of Fogo can be subdivided into four phases: (1) The uplifted Seamount Series (~4.5 Ma) consists of carbonatites and alkaline basalts. (2) The first subaerial lavas of the Monte Barro Group, which lacks absolute age constraints, unconformably overlie the carbonatites. (3) The main phase of intense volcanism, the 2–3-km-thick Monte Amarelo Group, consists mainly of highly alkaline basic to intermediate lavas and scoria cones. These rocks may be entirely of Quaternary age. The Monte Amarelo phase ended with a giant lateral collapse between 123 ka and 62 ka (Foeken et al. 2009), represented present-day by the up to 1 km high Bordeira cliff. (4) The post-collapse Cha das Caldeiras Group (62 ka to present) consists mainly of alkaline basanites to tephrites. This group includes a ~2-km-thick sequence infilling the collapse scarp (Cha das Caldeiras plain) to where most historic eruptions were restricted, and the Pico do Fogo.

Chronology of the 1995 eruption

The eruption lasted from April 2nd to May 26th, 1995, and was chemically and mineralogical zoned and bimodal in occurrence. In the first days of the eruption, tephriphonolitic to phonotephritic pyroclastics and lavas were discharged, followed by tephrites to basanites. For the sake of clarity, these groups will be referred to as phonotephrites and basanites throughout this paper. Detailed descriptions of the eruption chronology can be found in Réffega et al. (1997), Correia and Costa (1995), and in the reports of the Smithsonian Institution (GVNB v. 20, no. 3; no. 4; no. 5; no. 11/12); it is briefly summarized here.

Initial Strombolian activity occurred along a 200 m long radial fissure at the SW flank of Pico do Fogo (Fig. 1b). Pyroclastics started to build up a scoria cone named Pico Pequeno. On April 3rd, the fissure had extended to 2 km length, and the eruption style changed to Hawaiian with lava fountains up to 400 m high feeding a lava flow that cut the main road to Portela village. Seven vents were active along the main fissure, which consisted of one ENE-WSW radial fracture at Pico do Fogo and a NNE-SSW oriented segment at Monte Beco (Fig. 1b) that became sealed gradually by a lava flow. In addition to the main lava flow several pahoehoe lobes formed during the first 2 days. Hawaiian lava fountaining at Pico Pequeno continued until April 17th, then Strombolian activity dominated until the end of the eruption. On April 23rd, a new vent opened at the NW base of Pico Pequeno starting to erupt spatter and pahoehoe lava that spread over the earlier lavas. Volcanic activity continued with gradually decreasing effusion rates and short phases of intensified explosive action. At the end of the eruption on May 26th, an area of about 6.3 km^2 was covered by lava flows, and a total volume of about 54–68 $\times$ 10^6 m^3 of volcanic material had been erupted (Torres et al. 1997).

Precursory and coeval seismicity

Seismic events related to the 1995 eruption are described in detail in Heleno da Silva et al. (1997, 1999) and Heleno (2003) and are summarized briefly herein. In January and February 1994, a small seismic crisis occurred in the surroundings of Brava. Initially, the majority of earthquakes were located beneath the channel between Brava and Fogo, later on almost all events occurred beneath and W of Brava. The volcano-tectonic seismicity was interpreted to reflect magma movement. On Fogo itself, a swarm of unlocated microearthquakes toward the SW of the islands and volcanic tremor within the Cha das Caldeiras collapse structure were observed (Heleno and Fonseca 1999).

From March 25th, 1995 on, weak intermittent earthquakes were felt by the residents of Cha das Caldeiras. On 2nd April earthquakes became more frequent, and a stronger one in the evening was probably associated with the opening of the eruption fissure. Concomitant to the eruption, a weak volcanic tremor was felt on the floor of Cha das Caldeiras. On April 10th, seismicity increased probably due to temporary obstruction of the vent and two microearthquakes probably related to a change in eruptive style occurred on April 12th. Volcanic tremor remained moderate to strong until the end of the eruption, with episodes of increasing amplitude marking the larger events from April 18th to 19th when the eruptive style changed from dominantly Hawaiian to Strombolian. Immediately

after the end of the eruption, a swarm of seismic events occurred, interpreted as interaction between phreatic fluids and the retreating magma.

Petrography

We have investigated 11 samples of various eruption products covering the entire temporal and chemical variation of the eruption. Table 1 gives an overview of the sample localities and the major and trace element composition. Table 2 contains clinopyroxene data used for clinopyroxene-melt-thermobarometry. Additional chemical data of the 1995 and other Fogo eruptions are published by Munhá et al. (1997), Silva et al. (1997), Kokfelt (1998), Doucelance et al. (2003), and Escrig et al. (2005). Modal proportions were estimated visually by area in thin sections and hand specimen.

Table 1 Major (wt%) and trace element (ppm) analyses of 1995 eruption products

Sample	Fogo 08	Fogo 09	Fogo 11	Fogo 12	Fogo 13	Fogo 15	Fogo 60	Flow 95	PicoLap95
Rock type	Phonoteph	Phonoteph	Phonoteph	Tephrite	Tephrite	Basanite	Phonoteph	Basanite	Basanite
Description	Lapilli	Bomb	Bomb	Bomb	Bomb	Lava	Lava	Lava	Lapilli
Chronology	Early	Early	Early	Early?	Very late	Late	Early	Middle	Middle?
Lati (N)	14°56.19′	14°56.15′	14°56.15′	14°56.16′	14°56.58′	14°56.58′	14°56.84′	14°56.31′	14°57.62′
Long (W)	24°21.65′	24°21.70′	24°21.70′	24°21.65′	24°21.28′	24°21.80′	24°21.67′	24°21.54′	24°21.95′
Major elements									
SiO_2	46.72	48.91	48.82	42.34	42.86	43.11	47.76	42.37	42.97
TiO_2	2.52	2.05	2.07	3.58	3.55	3.50	2.24	3.69	3.35
Al_2O_3	18.67	19.73	19.65	15.88	15.53	15.75	19.14	15.12	15.08
Fe_2O_3t	8.91	7.92	7.93	12.68	13.04	12.85	8.68	13.63	13.11
MnO	0.23	0.20	0.20	0.22	0.19	0.19	0.20	0.19	0.20
MgO	2.59	2.37	2.40	5.20	6.09	5.97	2.79	6.61	6.86
CaO	8.34	7.00	7.00	11.56	11.59	11.26	7.69	11.90	10.45
Na_2O	6.44	6.50	6.46	4.49	4.09	4.12	6.22	3.75	3.95
K_2O	4.34	4.44	4.45	3.15	2.74	2.84	4.18	2.58	2.71
P_2O_5	0.64	0.57	0.57	1.09	0.97	0.96	0.68	0.95	1.06
H_2O	0.45	0.38	0.39	0.23	0.31	0.30	0.60	0.30	1.04
CO_2	0.05	0.04	0.05	0.05	0.04	0.04	0.08	0.05	0.18
Total	99.90	100.1	99.99	100.5	101.0	100.9	100.3	101.1	100.9
Mg#	40.39	41.09	41.36	48.87	52.12	51.99	42.83	53.06	54.95
Trace elements									
Li	16.76	16.67		10.43	8.97	9.06	14.61	8.58	10.20
Sc	4.29	3.92		16.99	26.07	23.74	4.96	28.01	18.58
V	257	184		365	371	358	202	391	332
Cr	0.7	4.0		16.4	82.4	63.8	7.0	88.8	41.1
Co	16.6	14.4		34.6	39.9	38.3	16.8	43.8	41.7
Ni	1.94	2.64		22.27	42.62	39.94	3.33	50.61	63.97
Cu	13.12	10.46		46.10	58.01	57.35	12.24	64.24	47.09
Zn	133	115		139	124	110	125	116	117
Ga	27.7	26.9		25.9	25.4	25.3	26.4	25.4	23.8
Rb	123.7	129.4		84.9	74.0	77.4	117.4	70.3	72.8
Sr*	1597	1409	1408	1277	1059	1095	1380	1009	1055
Y	37.7	30.9		37.3	31.2	31.4	31.1	31.4	31.1
Zr*	640	533	529	517	413	416	521	390	402
Nb	176	155		133	103	106	147	99	104
Cs	1.44	1.42		0.96	0.80	0.82	1.31	0.75	0.82
Ba*	1259	1214	1219	957	882	867	1196	771	835
La	92.6	85.8		75.0	63.1	65.0	83.9	60.5	64.1

Table 1 continued

Sample	Fogo 08	Fogo 09	Fogo 11	Fogo 12	Fogo 13	Fogo 15	Fogo 60	Flow 95	PicoLap95
Ce	183	165		159	133	135	164	129	135
Pr	20.4	17.9		19.0	15.8	15.9	18.2	15.5	16.1
Nd	74.3	63.2		72.2	60.3	60.7	65.7	60.4	61.4
Sm	13.5	11.2		14.6	12.6	12.2	11.9	12.3	12.2
Eu	4.09	3.44		4.33	3.70	3.69	3.67	3.66	3.74
Gd	11.07	9.19		12.09	10.14	10.40	9.44	10.36	10.49
Tb	1.45	1.19		1.53	1.29	1.30	1.29	1.32	1.29
Dy	8.08	6.66		8.12	6.84	6.80	7.33	7.08	6.80
Ho	1.48	1.19		1.48	1.19	1.19	1.25	1.22	1.20
Er	3.86	3.24		3.55	3.03	3.05	3.27	2.99	3.03
Tm	0.50	0.41		0.45	0.39	0.39	0.43	0.40	0.40
Yb	2.92	2.60		2.69	2.21	2.22	2.60	2.20	2.08
Lu	0.45	0.36		0.41	0.32	0.32	0.38	0.32	0.31
Hf	10.48	9.40		9.63	9.64	9.68	9.38	8.54	8.20
Ta	9.32	8.57		7.61	5.78	5.91	8.26	5.72	6.01
Pb	6.62	6.09		3.98	3.40	3.56	5.93	3.08	3.60
Th	8.26	8.66		5.41	4.81	5.05	8.15	4.47	4.86
U	2.09	2.15		1.34	1.13	1.17	2.01	1.05	1.13

* Denotes trace elements analyzed by XRF, all others by ICP-MS. Mg# corresponds to a $Fe_2O_3/FeO = 0.3$ ($Fe^{2+}/Fe = 0.79$) based on the data of Kokfelt (1998)

Early erupted phonotephrites

The phonotephrites consist of a glassy to microcrystalline matrix interspersed with 1–15 vol.% of phenocrysts and microphenocrysts (≤3 mm). The major phenocryst phase is euhedral Ti–rich aluminian diopside (up to 10 vol.%, Mg# 63.4–72.4; Mg# = molar Mg/(Mg + Fe)*100) followed by rounded kaersutitic amphibole (1–5 vol.%) and Ti–Mg–Al-rich magnetite (2–3 vol.%). Rare olivine and plagioclase are partly corroded and interpreted as xenocrysts. The groundmass consists of clinopyroxene and Ti–Mg–Al-rich magnetite with subordinate feldspar, melilite, and amphibole in varying amounts. Apatite occurs as columnar inclusions in clinopyroxene and amphibole phenocrysts.

Basanites

Basanites to tephrites of the 1995 eruption range in their normative olivine content from 7.0 to 13.6% (using $Fe^{3+}/Fe^{2+} = 0.12$ based on analyses of Kokfelt (1998)). The samples consist of a glassy to microcrystalline groundmass interspersed with phenocrysts (≤3 mm) and microphenocrysts of euhedral Ti–rich aluminian diopside (~20 vol.%, Mg# 67.3–74.2), euhedral olivine (2–5 vol.%, Mg# 76.5–83.5), Ti–Mg–Al-rich magnetite (~5 vol.%) and kaersutitic amphibole (0–5 vol.%). Microlite phases are comprised of clinopyroxene, Ti–Mg–Al-rich magnetite, and subordinate melilite, plagioclase, and olivine. Many clinopyroxene phenocrysts reveal hour-glass zonations or show articulate thin zonations at the outermost rims. A few clinopyroxenes contain older rounded cores of similar color to the rim zones; green cores are very rare. Some clinopyroxene phenocrysts contain apatite inclusions. Sparse groundmass leucite was described for tephrites of 1995 by Munhá et al. (1997) but was not observed in the studied samples.

Xenoliths and xenocrysts are very rare in the products of the 1995 eruption and are restricted to a few small clasts of pyroxenites and pyroxene-hornblendites occurring predominantly in the late lavas.

Occurrence of fluid inclusions

CO_2-rich fluid inclusions occur in some clinopyroxene and olivine phenocrysts and are partly associated with melt inclusions. We investigated both primary inclusions occurring isolated or in randomly oriented groups that were incorporated during growth of phenocrysts, and trails of secondary and pseudosecondary inclusions incorporated in healed cracks (Roedder 1984) (Fig. 2). Secondary inclusions are more abundant than primary inclusions in the studied samples but intersections of secondary inclusion trails are rare. Most fluid inclusions are mature and spherical to oval or have the host crystal shape. The investigated inclusions are up to 21 μm in size with a majority around 2–6 μm. Products of secondary reactions between trapped fluid and the

Table 2 Mean compositions of clinopyroxene rims (wt%) used for cpx-melt-thermobarometry

Sample_#	SiO_2	TiO_2	Al_2O_3	FeO	MnO	MgO	CaO	Na_2O	Cr_2O_3	Total	Mg#	P [MPa]	T [°C]
Basanites													
Flow95_01	41.46	4.51	10.80	8.24	0.13	10.94	22.31	0.44	0.01	98.8	70.3	530	1096
Flow95_12	42.36	4.73	10.96	8.01	0.14	10.85	22.27	0.45	0.01	99.8	70.7	540	1098
Flow95_15	41.15	4.75	11.63	8.14	0.11	10.63	22.32	0.45	0.01	99.2	70.0	550	1099
Flow95_16	42.99	4.04	9.90	7.85	0.13	11.41	22.29	0.45	0.01	99.1	72.2	520	1094
Flow95_17	42.42	4.36	10.72	7.93	0.12	11.18	22.31	0.43	0.01	99.5	71.5	510	1096
Flow95_18	44.28	3.82	9.70	7.73	0.15	11.49	22.21	0.46	0.01	99.9	72.6	540	1096
Flow95_19	44.66	3.62	8.83	7.68	0.12	12.13	22.43	0.40	0.00	99.9	73.8	460	1087
Flow95_22	41.57	4.63	11.11	8.32	0.12	10.78	22.18	0.46	0.01	99.2	69.8	560	1099
Flow95_23	43.94	3.48	9.33	7.50	0.11	11.98	22.59	0.42	0.02	99.4	74.0	490	1090
Flow95_26	43.79	3.84	9.79	7.77	0.12	11.71	22.40	0.44	0.01	99.9	72.9	510	1093
PLap95_15	43.51	3.79	9.54	7.84	0.14	11.66	22.46	0.45	0.01	99.4	72.6	520	1088
PLap95_21	41.89	4.42	10.78	8.29	0.13	10.90	22.33	0.47	0.00	99.2	70.1	550	1093
PLap95_27	42.82	4.08	9.94	8.06	0.15	11.30	22.44	0.44	0.00	99.2	71.4	510	1088
Fogo12_03	40.13	5.50	11.83	8.74	0.14	10.09	22.38	0.55	0.00	99.4	67.3	680	1083
Fogo12_07	43.41	3.90	9.68	7.69	0.13	11.60	22.83	0.47	0.01	99.7	72.9	580	1071
Fogo12_09	42.38	4.35	10.56	8.03	0.16	10.77	22.67	0.54	0.01	99.5	70.5	650	1078
Fogo12_10	40.52	5.03	11.57	8.63	0.15	10.26	22.42	0.54	0.00	99.2	67.9	670	1082
Fogo12_11	40.76	5.16	11.59	8.58	0.13	10.27	22.48	0.55	0.01	99.6	68.1	680	1083
Fogo12_12	42.67	4.25	10.35	8.16	0.16	10.87	22.68	0.53	0.01	99.7	70.4	640	1077
Fogo12_19	43.70	3.80	9.52	7.63	0.11	11.74	22.76	0.46	0.01	99.8	73.3	570	1070
Fogo12_20	42.21	4.44	10.46	8.36	0.17	10.99	22.61	0.49	0.00	99.8	70.1	610	1075
Fogo13_04	44.60	3.72	9.46	7.62	0.17	11.84	22.41	0.44	0.01	100.3	73.5	580	1118
Fogo13_06	43.56	4.01	10.27	7.72	0.12	11.43	22.52	0.45	0.01	100.1	72.5	600	1120
Fogo13_09	42.97	4.24	10.81	7.89	0.14	11.10	22.50	0.49	0.01	100.2	71.5	640	1124
Fogo13_10	43.34	4.16	10.46	7.81	0.14	11.45	22.42	0.48	0.00	100.3	72.3	620	1122
Fogo13_11	43.18	4.20	10.58	7.81	0.15	11.31	22.47	0.46	0.01	100.2	72.1	610	1122
Fogo13_13	43.13	4.21	10.49	7.85	0.12	11.46	22.53	0.45	0.01	100.3	72.2	590	1120
Fogo13_14	44.31	3.71	9.49	7.51	0.14	11.80	22.36	0.47	0.01	99.8	73.7	600	1119
Fogo13_15	44.46	3.87	9.61	7.58	0.16	11.76	22.45	0.45	0.01	100.3	73.4	590	1118
Fogo13_17	45.08	3.58	9.12	7.55	0.12	12.15	22.55	0.44	0.00	100.6	74.2	570	1116
Fogo13_18	42.36	4.48	11.29	7.96	0.13	10.92	22.47	0.49	0.00	100.1	71.0	640	1125
Fogo13_19	42.92	4.32	11.31	7.73	0.14	11.03	22.40	0.50	0.00	100.4	71.8	650	1127
Fogo13_20	44.91	3.56	9.68	7.62	0.16	11.84	22.51	0.48	0.01	100.8	73.5	610	1120
Fogo13_23	44.03	3.98	10.16	7.69	0.16	11.67	22.44	0.47	0.01	100.6	73.0	610	1121
Fogo13_24	43.21	4.27	10.82	7.84	0.15	11.31	22.49	0.48	0.01	100.6	72.0	630	1124
Fogo13_25	44.79	3.70	9.25	7.62	0.15	12.15	22.44	0.43	0.01	100.6	74.0	560	1116
Fogo13_26	43.04	4.27	10.85	7.82	0.14	11.29	22.45	0.47	0.01	100.4	72.0	620	1123
Fogo13_28	43.09	4.29	10.80	7.76	0.12	11.31	22.44	0.49	0.01	100.3	72.2	640	1124
Fogo13_29	43.20	4.00	10.37	7.71	0.14	11.46	22.63	0.46	0.01	100.0	72.6	610	1120
Fogo13_31	42.81	4.36	10.58	7.93	0.13	11.36	22.38	0.46	0.01	100.0	71.9	610	1122
Fogo13_33	42.35	4.39	11.21	7.66	0.12	11.00	22.50	0.49	0.00	99.8	71.9	640	1125
Fogo13_34	43.84	3.87	9.90	7.64	0.15	11.63	22.41	0.46	0.01	100.0	73.1	610	1120
Fogo13_35	43.83	3.73	9.30	7.54	0.15	11.76	22.61	0.46	0.01	99.4	73.5	590	1117
Fogo13_37	43.59	3.89	9.68	7.76	0.14	11.78	22.42	0.44	0.01	99.8	73.0	580	1118
Fogo14_04	41.94	4.66	11.16	8.14	0.11	10.77	22.55	0.45	0.01	99.8	73.7	540	1097
Fogo14_07	42.41	4.58	11.25	7.82	0.11	10.78	22.70	0.45	0.01	100.1	71.1	530	1097
Fogo15_01	43.07	4.03	10.24	7.67	0.14	11.19	22.21	0.47	0.00	99.0	72.2	620	1116

Table 2 continued

Sample_#	SiO_2	TiO_2	Al_2O_3	FeO	MnO	MgO	CaO	Na_2O	Cr_2O_3	Total	Mg#	P [MPa]	T [°C]
Fogo15_07	42.70	4.30	10.92	7.66	0.14	10.86	22.31	0.50	0.01	99.4	71.6	650	1119
Fogo15_10	42.87	4.23	10.20	7.87	0.13	11.19	22.12	0.45	0.00	99.1	71.7	600	1115
Fogo15_11	43.94	3.80	9.55	7.58	0.15	11.58	22.36	0.45	0.01	99.4	73.1	590	1112
Fogo15_12	43.25	4.08	9.97	7.72	0.14	11.31	22.46	0.46	0.01	99.4	72.3	600	1113
Fogo15_14	43.05	4.18	10.26	7.49	0.14	11.20	22.43	0.46	0.00	99.2	72.7	610	1114
Fogo15_16	43.02	4.25	10.58	7.56	0.15	11.05	22.33	0.48	0.01	99.5	72.3	630	1117
Fogo15_19	42.11	4.45	10.99	7.90	0.13	10.85	22.37	0.49	0.01	99.3	71.0	650	1119
Fogo15_21	44.37	3.67	9.34	7.52	0.15	11.67	22.46	0.44	0.01	99.7	73.4	580	1111
Fogo15_24	42.40	4.45	10.79	7.91	0.14	10.98	22.34	0.47	0.01	99.5	71.2	620	1117
Phonotephrites													
Fogo09_01	43.55	3.22	9.49	9.20	0.23	10.62	22.27	0.59	0.00	99.2	67.3	520	1013
Fogo09_02	43.39	3.39	9.82	8.81	0.21	10.46	22.48	0.60	0.00	99.2	67.9	520	1013
Fogo11_02	43.01	3.66	10.04	8.93	0.19	10.52	22.49	0.53	0.00	99.4	67.7	480	1011
Fogo11_03	43.24	3.63	9.89	8.60	0.18	10.77	22.58	0.55	0.01	99.5	69.1	490	1011
Fogo11_08	43.81	3.39	9.57	8.91	0.24	10.74	22.45	0.55	0.00	99.7	68.2	490	1011
Fogo11_10	42.75	3.78	10.09	9.02	0.22	10.44	22.45	0.56	0.01	99.4	67.4	500	1012
Fogo11_14	43.30	3.49	9.76	8.55	0.19	10.80	22.36	0.55	0.00	99.0	69.2	490	1011
Fogo60_01	44.69	3.33	8.92	7.93	0.15	11.69	22.42	0.51	0.01	99.7	72.4	450	1030
Fogo60_05	42.38	3.86	10.23	9.02	0.22	10.30	22.09	0.55	0.01	98.7	67.1	510	1037
Fogo60_07	42.67	3.91	10.14	8.88	0.16	10.70	22.13	0.55	0.01	99.2	68.2	510	1037

Each sample comprises the mean value of 5–20 analyzed points of one clinopyroxene phenocryst. P and T calculated after Putirka et al. (2003)

Table 3 Compositions of glasses used for clinopyroxene-melt thermobarometry determined by EMP and calculated (*) by crystal fractionation modeling of observed phenocryst phases

Melt	Used for	SiO_2	TiO_2	Al_2O_3	FeO	MnO	MgO	CaO	Na_2O	K_2O	P_2O_5	Total
Basanites												
Flow95	Flow95, Fogo 14	44.92	3.31	18.08	10.50	0.24	3.80	9.84	5.02	3.43	1.24	100.38
PicoLap95	PicoLap95	45.83	2.94	18.38	9.55	0.24	3.68	9.18	5.17	3.60	1.23	99.79
Fogo 12*	Fogo 12	44.04	3.08	17.84	10.90	0.24	3.47	9.06	5.78	4.15	1.45	100.00
Fogo 13*	Fogo 13	44.22	3.30	17.06	10.91	0.20	4.38	10.54	4.89	3.32	1.18	100.00
Fogo 15*	Fogo 15	44.58	3.23	17.33	10.71	0.20	4.27	10.15	4.93	3.44	1.17	100.00
Tephriphonolites												
Fogo 11*	Fogo 11, 09	50.54	1.88	20.52	6.45	0.20	2.02	6.40	6.87	4.75	0.39	100.00
Fogo 60*	Fogo 60	49.40	2.06	19.97	7.23	0.20	2.42	7.14	6.62	4.46	0.50	100.00

inclusion wall were not observed in any inclusion. A few large primary inclusions show textures of partial decrepitation such as small crystallographically oriented cracks or trails of microinclusions radiating from inclusions; these were not included in our analyses.

Analytical Methods

Fluid inclusions were examined in 100-µm-thick doubly polished sections of lavas and pyroclastics. Microthermometric measurements were carried out using a Linkam® THMSG 600 heating–cooling stage at the Department of Geosciences, University of Bremen, calibrated with SYNFLINC® synthetic fluid inclusion standards at −56.6°C (triple point of CO_2), 0.0°C and 374.1°C (H_2O). Precision of melting and homogenization temperatures as determined by repeated measurements of standards and samples is ±0.2°C or better. The standard data as well as some inclusions showing critical behavior at +31.1°C indicate that the accuracy is also ±0.2°C. Densities of CO_2 inclusions were calculated using the auxiliary equations 3.14 and 3.15 of Span and Wagner (1996); the results closely match those obtained by the Angus et al. (1976) equations.

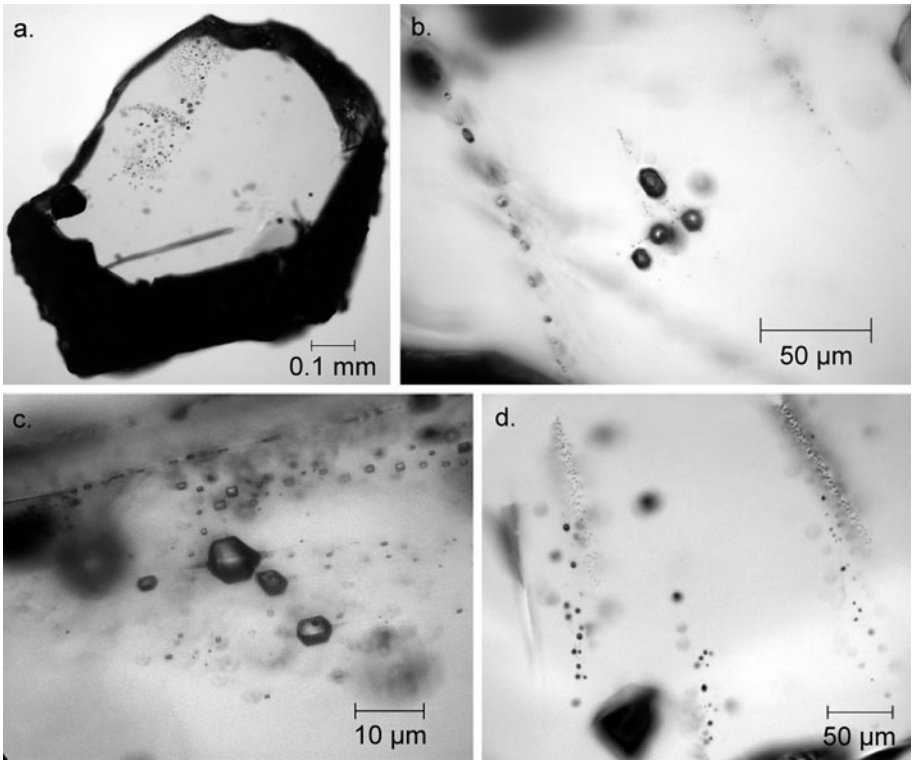

Fig. 2 Photomicrographs of fluid inclusions (FI) in phenocrysts. **a** Olivine from a basanitic sample (Fogo 15) showing trails of secondary inclusions in the upper left part. **b** Group of large primary FI in olivine of a basanitic sample (Fogo 13) with visible CO_2 bubbles and halos of minute inclusions resulting from decrepitation; these were not incorporated in our analyses. FI have negative crystal shape. Two trails of small melt inclusions crosscut the mineral. **c** Group of primary FI in olivine of a phonotephritic sample (Fogo 11). The large FI in the center and the one to the lower right show traces of decrepitation. In the upper part of the photograph trails of small secondary, FI and melt inclusions crosscut the mineral. **d** Various trails of secondary FI crosscutting a clinopyroxene phenocryst (sample Fogo 09)

Isochores and pressures were computed implementing the Sterner and Pitzer (1994) equation of state (EOS) for the CO_2–H_2O system. This EOS yields pressures almost identical to the frequently used EOS by Kerrick and Jacobs (1981) for densities below 0.8 g/cm^3 and performs better than the EOS by Holloway (1981) and Bottinga and Richet (1981) based on a smaller data set. See Hansteen and Klügel (2008) for a comparison of different equations of state for fluid inclusion barometry.

Major element analyses of minerals and glasses were performed with a JEOL JXA 8200 electron microprobe (EMP) at IFM-GEOMAR, Kiel. Analytical conditions included a focused beam with a current of 10–20 nA for mineral phases at an acceleration voltage of 15 kV. Glasses were analyzed with a defocused beam of 5–10 µm and a current of 10 nA. Analytical precision and accuracy were monitored by regular analysis of standard reference materials; see Table A1 in the electronic appendix. For diffusion calculations, semi-quantitative traverses across olivines were recorded with a focused beam of 100 nA, a spacing of 0.5 microns, and a dwell time of 1 s per point.

Whole-rock analyses of major elements, Sr, Ba, and Zr were performed at IFM-GEOMAR using a Philips X'Unique PW 1480 X-ray fluorescence spectrometer; H_2O and CO_2 were analyzed with a Rosemount CSA 5003 infrared spectrometer. All other trace elements were analyzed with a Thermo Finnigan Element2 ICP-MS at the Department of Geosciences, University of Bremen. See Duggen et al. (2009) for details on the analytical methods, and Tables A2 and A3 in the electronic appendix for analyses of standard reference materials accompanying the whole-rock analyses.

Sr–Nd–Pb isotope analyses were carried out at IFM-GEOMAR on 0.5–2 mm sized rock chips that were picked under a binocular microscope to eliminate visual signs of alteration. Depending on Sr–Nd–Pb concentrations, between 50 and 150 mg of sample chips were weighted into Savillex© Teflon beakers. To minimize the effects of sample handling the material was leached in ultra-pure 2 N HCl at 70°C for 1 h and subsequently rinsed three times in ELGA© water. The leached chips were then dissolved for 2 days in a 5:1 mixture of ultra-pure HF and HNO_3 at 150°C and ion exchange procedures followed established standard procedures (Hoernle et al. 2008). Isotope analyses were carried out in static multi-collection mode on a Finnigan MAT 262 RPQ2 + (Pb) and on a Thermo Finnigan TRITON-TI (Sr, Nd) thermal ionization mass spectrometer (TIMS). Sr and Nd isotopic ratios were normalized within run to $^{86}Sr/^{88}Sr = 0.1194$ and $^{146}Nd/^{144}Nd = 0.7219$, respectively, and all errors are reported as 2 sigma of the mean. NBS987 measured along with the samples gave $^{87}Sr/^{86}Sr = 0.710239 \pm 0.000014$ ($n = 4$) and was normalized to $^{87}Sr/^{86}Sr = 0.710250$. During two subsequent Nd-sessions La Jolla measured along with the samples gave $^{143}Nd/^{144}Nd = 0.511849 \pm 0.000008$ ($n = 12$) and $^{143}Nd/^{144}Nd = 0.511846 \pm 0.000007$ ($n = 12$) and were normalized to $^{143}Nd/^{144}Nd = 0.511850$. Although in this case, the measured Sr and Nd standard

Table 4 Sr–Nd–Pb (DS) data of Brava and Fogo samples

Sample	$^{87}Sr/^{86}Sr$	2σ	$^{143}Nd/^{144}Nd$	2σ	$^{206}Pb/^{204}Pb$	2σ	$^{207}Pb/^{204}Pb$	2σ	$^{208}Pb/^{204}Pb$	2σ	$^{207}Pb/^{206}Pb$	2σ	$^{208}Pb/^{206}Pb$	2σ
Brav 02	0.703681	(3)	0.512797	(3)	19.5186	(16)	15.5943	(14)	39.1923	(42)	0.79894	(2)	2.00794	(10)
Brav02*	0.703684	(2)	0.512793	(2)	19.5221	(15)	15.5977	(17)	39.2012	(55)	0.79898	(3)	2.00804	(14)
Brav 05	0.703549	(3)	0.512835	(3)	19.5502	(8)	15.5998	(7)	39.1934	(18)	0.79793	(1)	2.00476	(3)
Brav 06	0.703656	(3)	0.512820	(2)	19.5979	(6)	15.6075	(6)	39.1976	(17)	0.79638	(1)	2.00009	(4)
Brav 07	0.703534	(3)	0.512829	(5)	19.5936	(16)	15.6127	(12)	39.1799	(30)	0.79683	(2)	1.99963	(4)
Brav 08	0.703702	(2)	0.512783	(3)	19.4428	(13)	15.5960	(13)	39.1703	(44)	0.80215	(2)	2.01465	(10)
Brav 17	0.703443	(2)	0.512904	(3)	19.9111	(4)	15.6291	(3)	39.1722	(8)	0.78494	(1)	1.96736	(2)
Brav 18	0.703309	(3)	0.512918	(3)	19.8928	(11)	15.6357	(8)	39.1445	(19)	0.78600	(1)	1.96777	(4)
Brav 20	0.703592	(2)	0.512816	(3)	19.4324	(13)	15.5952	(15)	39.1146	(48)	0.80254	(2)	2.01286	(11)
Brav 21	0.703651	(2)	0.512793	(2)	19.3403	(8)	15.5999	(7)	39.0720	(20)	0.80660	(1)	2.02024	(5)
Brav 24	0.703636	(3)	0.512792	(3)	19.2857	(7)	15.5969	(6)	39.0176	(17)	0.80873	(1)	2.02314	(3)
Brav 25	0.703700	(3)	0.512787	(3)	19.4519	(11)	15.5941	(13)	39.1703	(42)	0.80168	(2)	2.01371	(11)
Brav 28	0.703593	(2)	0.512796	(2)	19.4605	(17)	15.5975	(14)	39.1139	(38)	0.80149	(2)	2.00991	(7)
Fogo 19	0.703520	(3)	0.512805	(2)	19.2729	(11)	15.5793	(12)	39.0146	(39)	0.80836	(2)	2.02432	(11)
Fogo 35	0.703519	(2)	0.512797	(3)	19.2624	(36)	15.5770	(39)	38.9995	(128)	0.80867	(7)	2.02464	(33)

Within run 2 sigma errors refer to last significant digits

values overlap with the normalized ratios, scaling to a fixed standard value ensures long-term comparability of Sr–Nd isotope data and therefore is a standard procedure of the IFM-GEOMAR laboratory. Pb isotope ratios were determined using the Pb double-spike (Pb-DS) technique. For details of the method, see Hoernle et al. (accepted with minor revisions). Pb (DS) values for NBS 981 ($n = 30$) and corresponding external 2sigma errors are $^{206}Pb/^{204}Pb = 16.9413 \pm 0.0019$, $^{207}Pb/^{204}Pb = 15.4995 \pm 0.0019$, $^{208}Pb/^{204}Pb = 36.7241 \pm 0.0048$, $^{207}Pb/^{206}Pb = 0.914891 \pm 0.000037$, and $^{208}Pb/^{206}Pb = 2.167719 \pm 0.000074$. Replicate analyses carried out as separate dissolution of sample "Brav 02" is within the errors of the standards.

Results

Whole-rock geochemistry

Major and trace elements

Major and trace element data of whole-rock analyses are reported in Table 1. Most bivariate plots reveal an articulate chemical bimodality between the early erupted phonotephrites and the later basanites (Fig. 3). Both rock groups have restricted major element compositions with e.g. Mg-contents ranging from 5.2 to 6.7 wt% in the basanites and from 2.4 to 2.8 wt% in the phonotephrites. The basanites also contain more Fe_2O_3(t), TiO_2, CaO, and P_2O_5, and less Al_2O_3 than the phonotephrites. The low concentrations of MgO, Ni (<64 ppm), and Cr (<89 ppm) of the most primitive rocks from the 1995 eruption clearly indicate that they represent not primitive magma but significant differentiation must have occurred at depth.

Trace element concentrations are similarly distinctive for the two rock groups. In phonotephrites, most incompatible elements (e.g. Sr, Ba, Zr, Rb, Nb, Pb, Th, U) are enriched compared to the basanites, whereas elements compatible in the observed phenocryst phases are depleted. The negative P and Ti anomalies in the phonotephrites most likely reflect removal of apatite and kaersutite + Ti–magnetite, respectively (Fig. 4). Rare earth element (REE) patterns are roughly similar for both rock types, but phonotephrites have higher La/Sm and lower Sm/Lu than the basanites and a concave-upward REE pattern, consistent with kaersutite fractionation.

Least-squares mass balance calculations were performed in order to test whether basanites and phonotephrites are related by fractional crystallization. Various compositions of basanites and phonotephrites were chosen for the calculations, all pairs yielded similar results. The lowest sum of squared residuals (0.109) was achieved by fractionating olivine (1.2 wt%), clinopyroxene (26.2 wt%), kaersutite (11.8 wt%), Ti–Mg–Al-rich magnetite (6.8 wt%) and apatite (1.5 wt%), which is consistent with our petrographic observations.

This model scenario of fractional crystallization was tested by calculating the concentrations of trace elements in the daughter melt and comparing them to the analyzed values. The calculations used partition coefficients compiled from the GERM database and proportions of fractionated minerals from the mass balance calculations. The respective data and the results are shown in Table A4 in the electronic appendix. Both batch- and Rayleigh-crystallization models

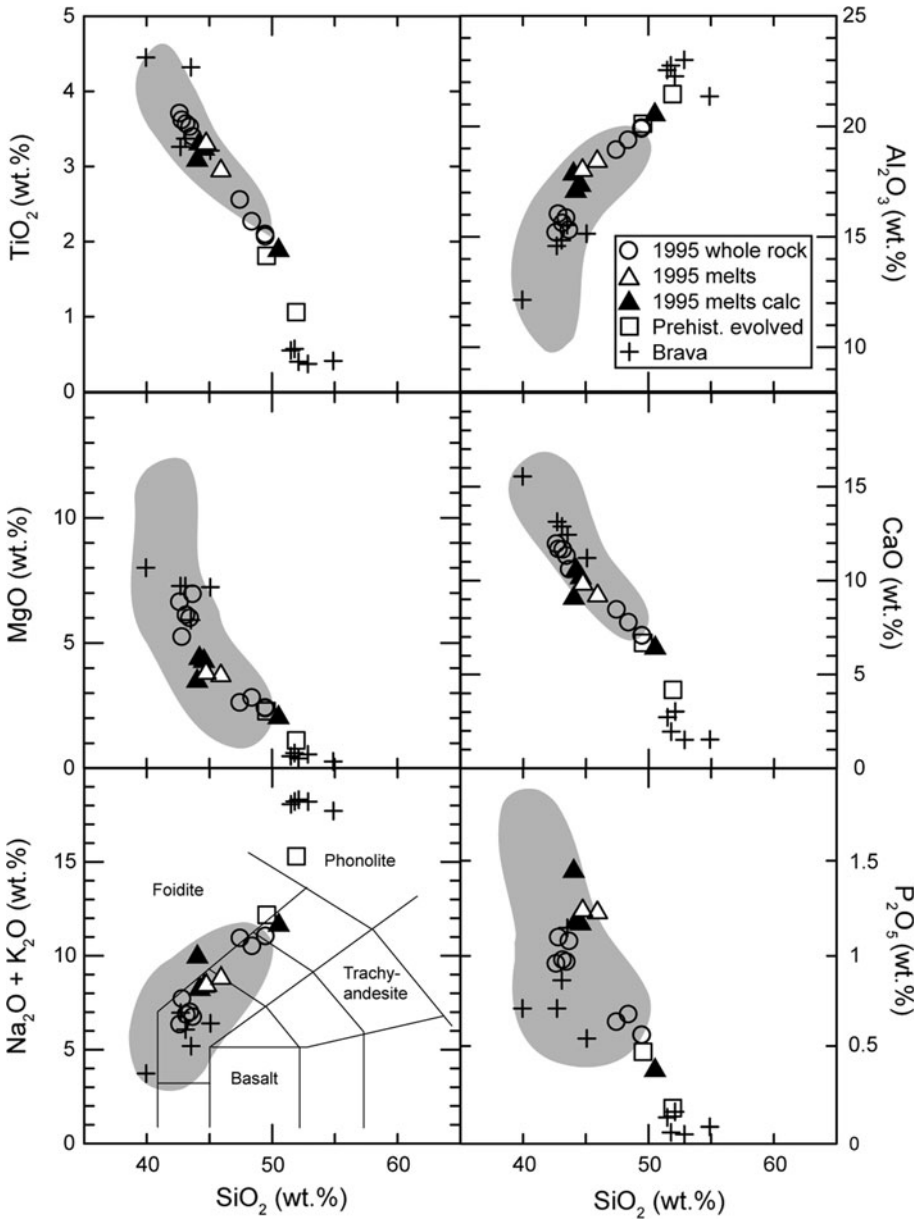

Fig. 3 Variations in major element compositions of samples from Fogo and Brava. Our data from the 1995 eruption are subdivided into whole-rock analyses (Table 1), and analyzed glasses and calculated melts (Table 3). Data for prehistoric evolved rocks and Brava rocks are presented in Table A1 in the electronic appendix. *Gray shaded* fields indicate the range of published Fogo data from historic and prehistoric rocks (Munhá et al. 1997; Kokfelt 1998; Doucelance et al. 2003; Escrig et al. 2005)

yield good to excellent agreement between calculated and analyzed concentrations in the daughter melt for most trace elements. We thus conclude that the 1995 phonotephrites are derived from the 1995 basanites through crystal fractionation, but the possibility that both represent two distinct melt batches cannot be ruled out.

Isotopic compositions of Fogo and Brava rocks

Radiogenic isotopes are an essential tracer for revealing similarities and differences between the mantle sources of Fogo and Brava, and for testing the hypothesis that the evolved 1995 magmas were contaminated by Brava melts. Isotope data have been published for historic and prehistoric Fogo rocks (Kokfelt 1998; Doucelance et al. 2003; Escrig et al. 2005) but are lacking for Brava and for the rare evolved Fogo rocks. We have therefore determined the Sr–Nb–Pb isotope ratios of 12 samples from Brava (two basanites from the Lower Unit, three basanites and seven phonolites from the Upper Unit; for stratigraphic units see Madeira et al. 2010) and of two prehistoric evolved rocks from Fogo. The elemental concentrations of these samples are shown in Table A5 and in Fig. 3, the isotope data are listed in Table 4 and shown in Fig. 5.

The 1995 basanites and phonotephrites are isotopically alike and do not indicate contamination of the phonotephrites by isotopically distinct material. The isotope ratios of the two evolved Fogo samples are similar to each other and plot within the well-defined arrays of published Fogo data. They differ strongly from the narrow fields of

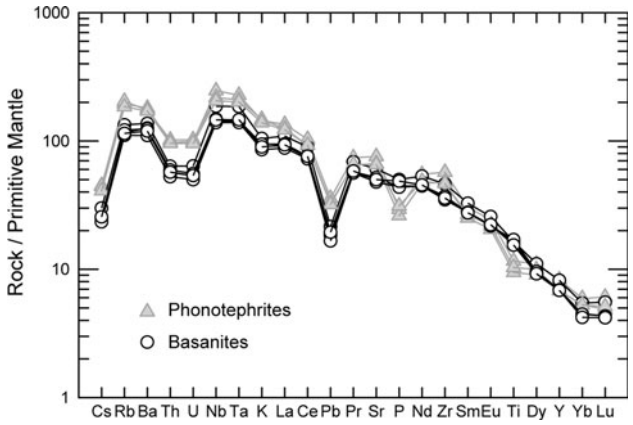

Fig. 4 Incompatible element diagram of investigated basanites and phonotephrites of the 1995 eruption, normalized to primitive mantle (Sun and McDonough 1989). Note the negative P and Ti anomalies of the phonotephrites reflecting apatite and amphibole fractionation, respectively

the 1995 eruptives by having lower $^{87}Sr/^{86}Sr$ and higher $^{143}Nd/^{144}Nd$, $^{206}Pb/^{204}Pb$, and $^{207}Pb/^{204}Pb$ ratios. The isotope ratios of the investigated Brava samples differ significantly from those of Fogo. The two Lower Unit samples show by far the lowest $^{87}Sr/^{86}Sr$ and the highest $^{143}Nd/^{144}Nd$, $^{206}Pb/^{204}Pb$, $^{207}Pb/^{204}Pb$ of the entire data set. The basanites and phonolites from the Upper Unit show $^{87}Sr/^{86}Sr$ ratios similar to Fogo rocks, but higher Nd and Pb ratios. Overall there is very little overlap between the fields for Fogo and for Brava rocks, which is indicative of distinct mantle sources and melting zones for both islands.

In summary, the combined isotope data show clearly that the 1995 basanites and phonotephrites show no affinity to phonolitic rocks from either Fogo or Brava (Fig. 5). This is a strong argument against a significant contribution of phonolitic melts from Brava to the evolved 1995 magmas. The isotope data are however consistent with the derivation of the 1995 phonotephrites from the basanites by crystal fractionation.

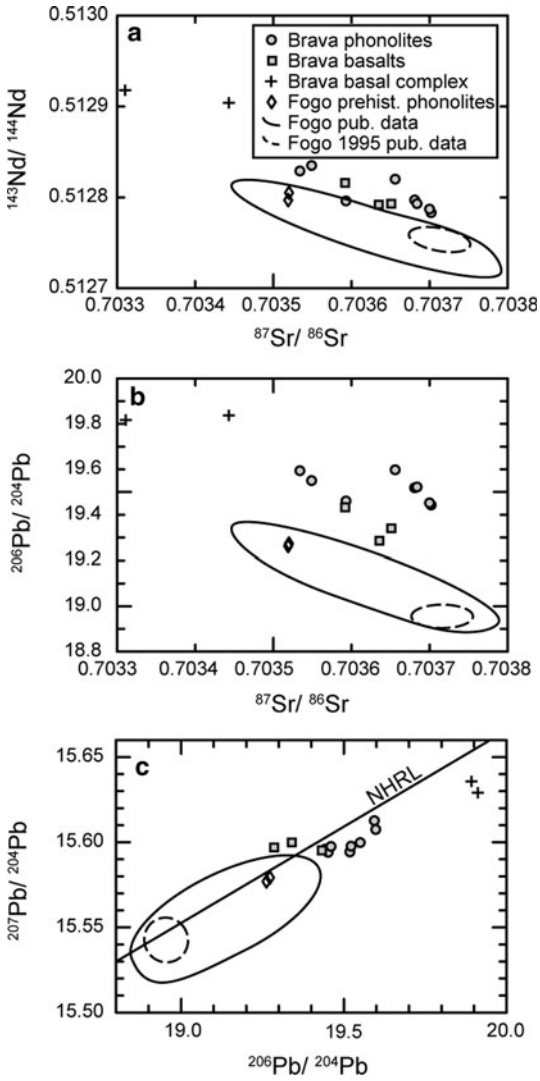

Fig. 5 Sr–Nd–Pb isotopic compositions of basaltic and phonolitic rocks from Brava and two prehistoric evolved rocks from Fogo compared to the array of published Fogo data from historic and prehistoric rocks (Kokfelt 1998; Doucelance et al. 2003; Escrig et al. 2005). The data indicate that the 1995 Fogo lavas cannot be derived by mixing of Fogo melts with Brava phonolites. Standard deviations (2σ) are smaller than symbol size. NHRL = Northern Hemisphere Reference Line (Hart 1984)

Microthermometry of fluid inclusions

Fluid inclusion compositions

We analyzed fluid inclusions in olivine (142 primary, 77 secondary inclusions) and clinopyroxene (13 primary, 94 secondary) phenocrysts of three basanitic and two phonotephritic samples of the 1995 eruption. All observed fluids froze to aggregates of solid CO_2 and vapor during cooling between −80 and −100°C. Further cooling to −190°C did not generate other phase transitions. During reheating, melting of fluids occurred between −57.2 and −56.2°C, close to the triple point of CO_2 (−56.6°C) (Fig. 6). Initial (T_i) and final melting (T_m) coincided in almost all cases; only two inclusions in olivine showed a melting interval of 0.2°C. Upon further heating all inclusions homogenized into the liquid phase below or at the critical point of pure CO_2 (31.1°C).

These data indicate that all investigated fluid inclusions consist of nearly pure CO_2, because significant amounts of components other than CO_2 would have caused a lowering of T_i and a melting interval rather than a triple point (Andersen and Neumann 2001; Frezzotti et al. 2002). Even if minor amounts of other phases like N_2 or CH_4 are present these would not significantly affect the interpretation of the

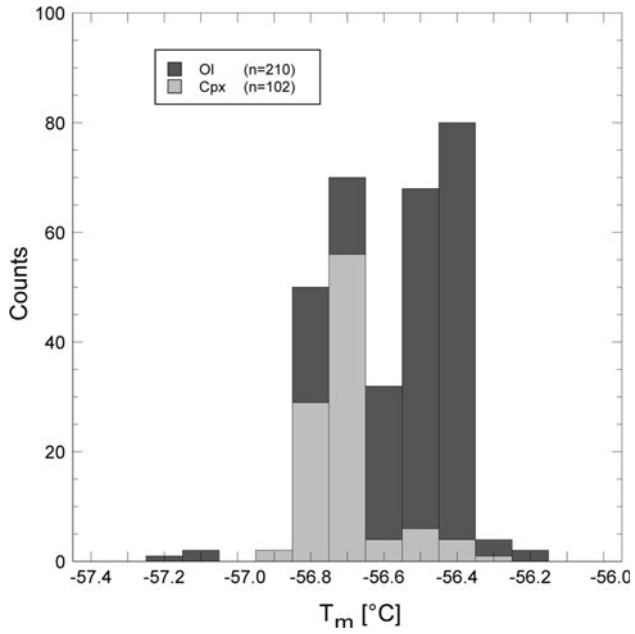

Fig. 6 Measured temperatures of final melting (T_m) of fluid inclusions in olivine and clinopyroxene phenocrysts indicate that most fluids are CO_2- dominated. Temperatures significantly below the melting temperature of pure CO_2 (−56.6°C) may indicate the minor presence of components such as N_2 or CH_4 in a few inclusions

PT conditions during fluid trapping (van den Kerkhof 1990). No evidence for H_2O was found in any observed inclusion although it is expected as a component of volatiles exsolved from basaltic melts (Dixon 1997). Either former H_2O became lost by hydrogen diffusion after fluid trapping (Bakker and Jansen 1991; Hollister 1990; Mackwell and Kohlstedt 1990) or it reacted with inclusion walls to form secondary minerals (Andersen and Neumann 2001; Frezzotti et al. 2002). No such reaction rims between fluid inclusions and host mineral could be observed, however.

Homogenization temperatures and densities of fluid inclusions

All inclusions homogenized into liquid CO_2 between 15.8 and 31.1°C (Fig. 7a). Not a single inclusion homogenized into the vapor phase, although great care was taken to find such inclusions. Whereas different microthermometric behavior of primary and secondary inclusions was not recognized, inclusions in clinopyroxene have a clear tendency to higher homogenization temperatures, and hence lower densities, than inclusions in olivine. Similar observations were made for fluid inclusions in volcanic rocks from the Canary Islands and were assigned to olivine being

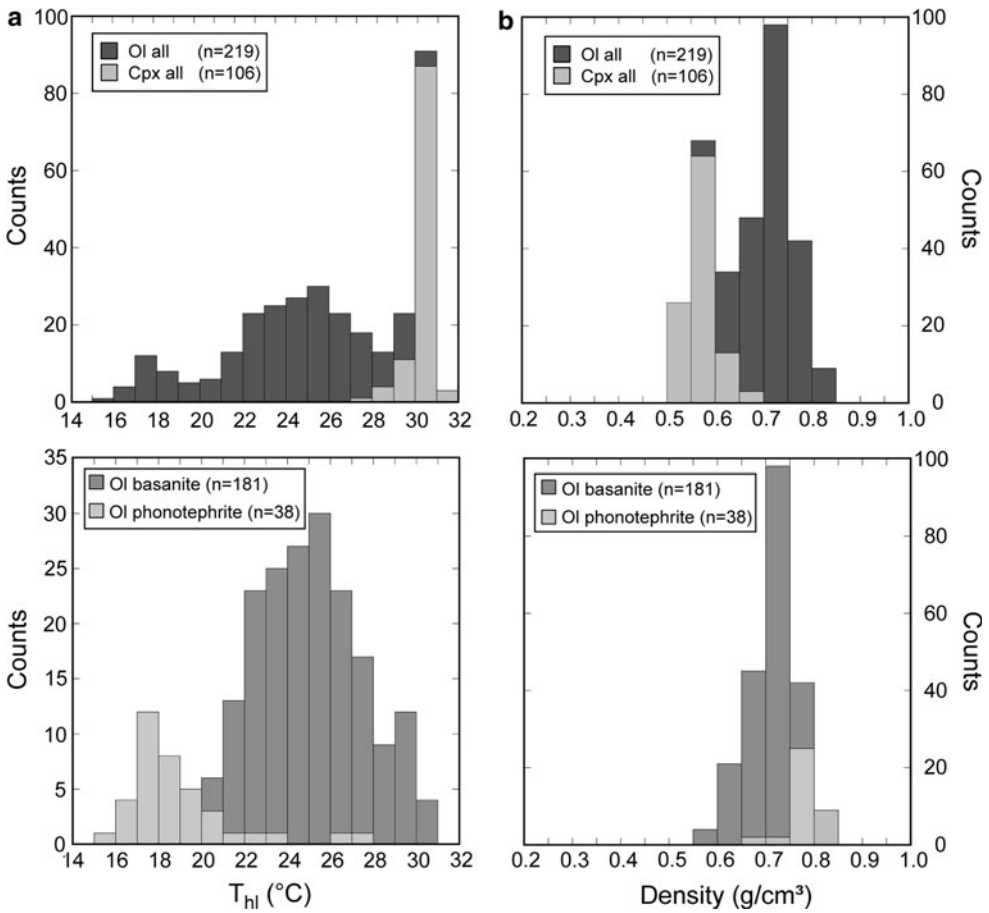

Fig. 7 **a** Measured homogenization temperatures T_{hl} and **b** calculated densities of CO_2-fluid inclusions in olivine and clinopyroxene phenocrysts in basanitic and phonotephritic samples. Upper panels (all inclusions) illustrate differences between olivine- and clinopyroxene-hosted inclusions; lower panels (only inclusions in olivine) illustrate differences between the two magma types. All inclusions homogenized into the liquid phase; *n* is the number of studied fluid inclusions

less prone to re-equilibration than clinopyroxene (Hansteen et al. 1998; Galipp et al. 2006).

For the basanites, inclusions in olivine ($n = 181$) homogenized between 20.6 and 30.3°C corresponding to densities of 0.58–0.77 g/cm^3, with a distinct frequency maximum at 0.64–0.76 g/cm^3 based on 90% of the values (Fig. 7b). Inclusions in clinopyroxene ($n = 2$) homogenized at 30.1 and 30.7°C (0.544 and 0.591 g/cm^3).

For the phonotephrites, inclusions in olivine ($n = 38$) show homogenization temperatures from 15.8 to 27.3°C corresponding to densities between 0.67 and 0.82 g/cm^3, with a distinct frequency maximum at 0.75–0.81 g/cm^3 based on 90% of the values. Inclusions in clinopyroxenes ($n = 104$) homogenized from 27.8–31.0°C equivalent to densities of 0.51–0.66 g/cm^3 with a frequency maximum between 0.52 and 0.61 g/cm^3.

Calculated pressures

Pressures of formation or re-equilibration of fluid inclusions were derived from isochores calculated using the equation of state for pure CO_2 of Sterner and Pitzer (1994). Model temperatures of 1,100°C for basanites and 1,030°C for tephriphonolites were chosen based on the results of clinopyroxene-melt geothermobarometry (see below). Temperature uncertainties have only minor influence on calculated pressures because of the moderately positive slopes of the calculated CO_2 isochores. For example, an uncertainty of ±20°C would transform into a pressure uncertainty of ±5–8 MPa. Olivine-hosted fluid inclusions in basanites yield a range of 265–443 MPa with 90% of the data between 300 and 440 MPa, and those in phonotephrites cover a range of 323–471 MPa with 90% between 400 and 470 MPa. Inclusions in clinopyroxene in phonotephrites yield a range of 202–313 MPa with 90% of data between 220 and 310 MPa (Fig. 8). Despite considerable overlap, the fluid inclusion data show clearly that (1) clinopyroxenes yield significantly lower pressures than olivines in the same rock and (2) the phonotephrites yield significantly higher pressures than the basanites. These observations place constraints on the interpretation of fluid inclusion data, as is discussed below.

Clinopyroxene-melt geothermobarometry

Temperatures and pressures of clinopyroxene crystallization were calculated by applying the clinopyroxene-melt geothermobarometer of Putirka et al. (2003), which is based on jadeite crystallization and jadeite-diopside + hedenbergite exchange equilibria. The thermobarometer was calibrated for a wide range of compositions, including hydrous and alkalic Si-undersaturated melts, and gave standard errors of estimate ± 33 K and ± 170 MPa for the regression data; a test data set between 0.1 and 4,000 MPa gave a SEE of 130 MPa.

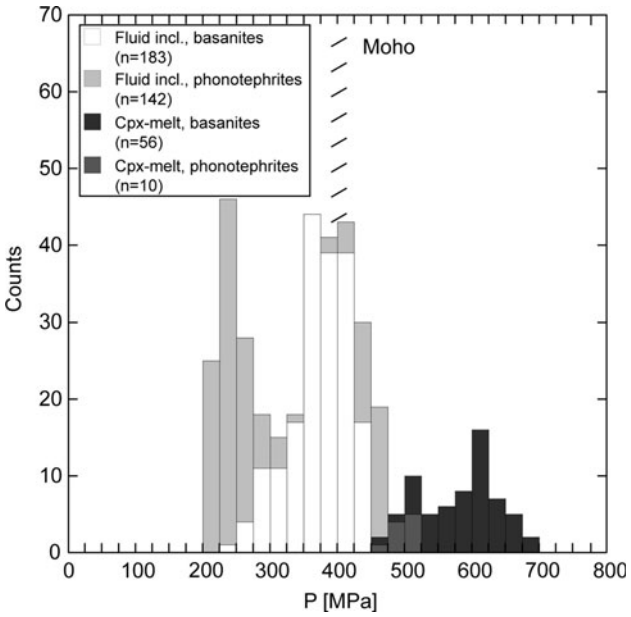

Fig. 8 Distribution of calculated pressures derived from fluid inclusion barometry in olivine and clinopyroxene phenocrysts and from clinopyroxene-melt barometry. Each data point of clinopyroxene-melt barometry corresponds to one clinopyroxene phenocryst. Pressure at Moho depth after the model of Pim et al. (2008)

Clinopyroxene compositions (Table 2) were determined by analyzing and averaging 4–20 points at a distance of 5–10 μm to the rim of euhedral phenocrysts. Clinopyroxenes showing sector zonation were avoided. For samples Flow 95 and PicoLap95, matrix glass compositions were analyzed directly with the microprobe. For all other samples possessing microcrystalline or microlite-rich matrixes, melt compositions were calculated by a mass balance subtracting the observed amount of phenocrysts from the respective whole-rock compositions (Table 3). This procedure is not critical to thermobarometry; for example, even a large relative error of 20% for the subtracted phenocryst contents would transform into P and T errors of less than 5 and 0.7% for olivine, and 2 and 1% for clinopyroxene, respectively.

Except for sample Fogo 12, all calculated melt compositions fall on the liquid line of descent for recent Fogo rocks (Fig. 3). The higher amount of alkalis in the Fogo 12 melt reflects the high alkali contents of the whole rock in combination with an exceptionally large amount of clinopyroxene phenocrysts. In order to test for chemical equilibrium between calculated melt and clinopyroxene rim compositions, the following criteria were applied:

(1) Test of Fe–Mg exchange equilibrium between clinopyroxene and melt. This test is not straightforward because $K_d = (X_{Fe*}/X_{Mg})_{Cpx}/(X_{Fe*}/X_{Mg})_{liq}$ was

highly variable in the calibration data of the thermobarometer (Fe* denotes total Fe). This is largely due to variable (in some cases not controlled) fO_2 and hence variable Fe^{3+}/Fe^{2+} in the respective experiments. As suggested by Putirka et al. (2003), we used a constant K_d of 0.275 for the equilibrium test. Another test was made using the empirical relation of Duke (1976).

$$\log\left(X_{Fe*}/X_{Mg}\right)_{Cpx} = -0.564 + 0.755 \times \log\left(X_{Fe*}/X_{Mg}\right)_{liq} \quad (1)$$

Clinopyroxenes with a discrepancy of >5% between the measured and both calculated Fe/Mg ratios were discarded (none in the basanites, 6 out of 16 in the phonotephrites).

(2) Test of measured clinopyroxene components (DiHd, EnFs, Jd, CaTs) matching those predicted by the clinopyroxene saturation model of Putirka (1999) within the $\pm$ 2σ level, following Putirka et al. (2003). All clinopyroxenes in basanites match these criteria. All clinopyroxenes in phonotephrites show systematic deviations of >2σ in the DiHd component but match the criteria for the EnFs, CaTs, and the pressure-sensitive Jd components quite well (Fig. A1). The systematic discrepancy of the DiHd component may be due to the sparse calibration data of the Putirka (2003) calibration for evolved Si-undersaturated melts. We decided to include the phonotephritic clinopyroxenes in our data set and note that the calculated pressures overlap those obtained for the basanites. The calculated pressures and temperatures are carefully interpreted, however.

Calculated pressures and temperatures

Clinopyroxene rims from basanitic samples of the 1995 eruption yield a pressure range of 460–680 MPa with a frequency maximum around ~600 MPa, well above the values shown by CO_2 fluid inclusions (Fig. 8). Clinopyroxene from phonotephritic samples yield a smaller pressure range of 460–520 MPa thus overlapping with the basanite data. They also overlap with the highest pressures indicated by fluid inclusions in the same rock type. Because the pressure at the Moho depth near Fogo is around 400 MPa as based on a crustal model by Pim et al. (2008), all pressures indicated by clinopyroxene-melt barometry reflect uppermost mantle depths. Calculated temperatures yield a range of 1,070–1,127°C for the basanites and 1,011–1,037°C for the phonotephrites (Fig. 9).

Model calculations show that the effect of analytical uncertainties is smaller than the prediction error of the thermobarometer and smaller than the overall data spread (Klügel et al. 2005). For the current data set, the pressure and temperature uncertainties due to analytical errors are estimated to be less than ±50 MPa and ±10°C (2σ).

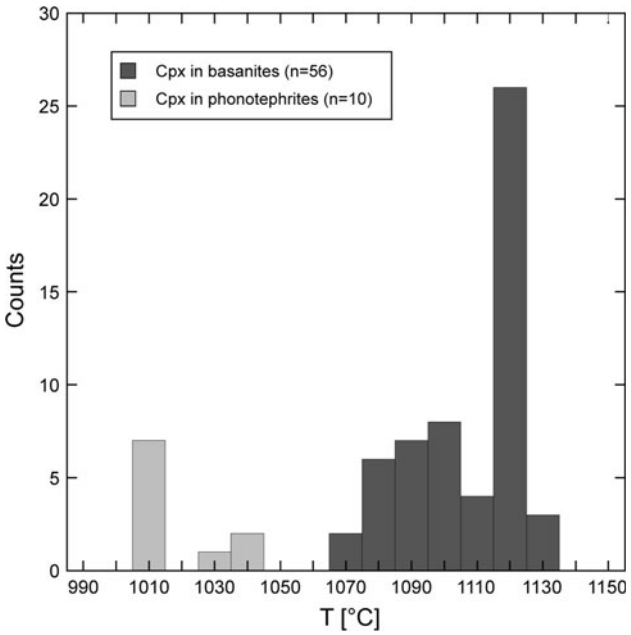

Fig. 9 Temperature distribution derived from clinopyroxene-melt equilibria in basanites and phonotephrites

Zonations of olivine phenocrysts

In order to place constraints on magma ascent dynamics during the eruption, we investigated the zonations of olivine phenocrysts by analyzing 36 semi-quantitative microprobe traverses across 25 euhedral crystals from two basanitic samples representing the main lava flow (Fogo 14) and the late pahoehoe unit (Fogo 15). In addition, a few quantitative profiles were analyzed to obtain accurate concentrations. All traverses were oriented perpendicular to the crystal rims in thin section; their exact orientation relative to the crystallographic axes was not determined.

Most olivines show simple normal zonations with a compositional plateau in the centers ($Fo_{81.5–82}$, 0.06–0.08 wt% NiO, 0.35–0.40 wt% CaO), and steep decrease in forsterite (Fo%) and NiO contents and increase in CaO near the rims. Some olivines are more complexly zoned, but reverse zonations are rare. The steep rim zonations indicate late-stage chemical disequilibrium between olivine and host melt caused by an event of rapidly decreasing Mg# and NiO and increasing CaO of the melt. This compositional change can be modeled by fractional crystallization of 4–5 wt% of olivine + clinopyroxene, and most plausibly reflects rapid microlite nucleation and crystal growth due to decompression-induced magma degassing

and undercooling during final ascent (e.g. Sparks and Pinkerton 1978). Because the resulting growth zonations cause solid-state diffusion in olivine, fitting of measured zonations by a pure diffusion model can yield upper limits for the actual times to produce them, which represent upper limits for the duration of final magma ascent to the surface (e.g. Klügel et al. 2000; Costa and Chakraborty 2004).

This being said, the simplest model for the rim zonations has the following initial and boundary conditions: olivines have an initially constant composition C_{core} ($t \leq 0$, $x \geq 0$) in equilibrium with the host melt, where t is time and x is the distance to the crystal-melt interface. At $t = 0$, the host melt composition changes instantaneously to cause a different but constant rim concentration C_{rim} ($t \geq 0$, $x = 0$). The resulting diffusion model is that of a semi-infinite half space with the solution

$$\frac{C - C_{rim}}{C_{core} - C_{rim}} = erf\frac{x}{2\sqrt{Dt}} \quad (2)$$

(Crank 1975). Most of the 46 analyzed Fo% zonations are well fitted by this simple equation, whereas the Ca zonations show larger scatter (owing to the low concentrations) and yield less satisfying fits. The semi-quantitative Ni data were too scattered as to be used for diffusion modeling. Profile lengths L were calculated from the error function fit as

$$L = 4\sqrt{Dt} \quad (3)$$

and range from 2.3 to 12.5 μm for Fo% and 1–4 μm for Ca (Fig. 10).

Duration of profile formation

For calculating diffusion times, we used a Fe–Mg interdiffusion coefficient $D_{FeMg} = 1.10 \times 10^{-16}$ m^2/s following the master equations of Dohmen and Chakraborty (2007) with the following parameters: oxygen fugacity of the melt = 3.49×10^{-5} Pa (calculated after Kress and Carmichael (1991) using $Fe^{3+}/Fe^{2+} = 0.12$), temperature = 1,100°C, and pressure = 600 MPa based on the data presented above. For Ca diffusion, we used $D_{Ca} = 7.84 \times 10^{-18}$ m^2/s calculated after Coogan et al. (2005). Both D_{FeMg} and D_{Ca} were calculated for [001], the direction of fastest diffusion.

Calculated diffusion times range from 0.8 to 24.7 h for Fo% and from 1.8 to 22.2 h for Ca zonations (one single outlier ignored). The majority of both data sets are between 1 and 13 h with a maximum frequency at 1–4 h for Fo%

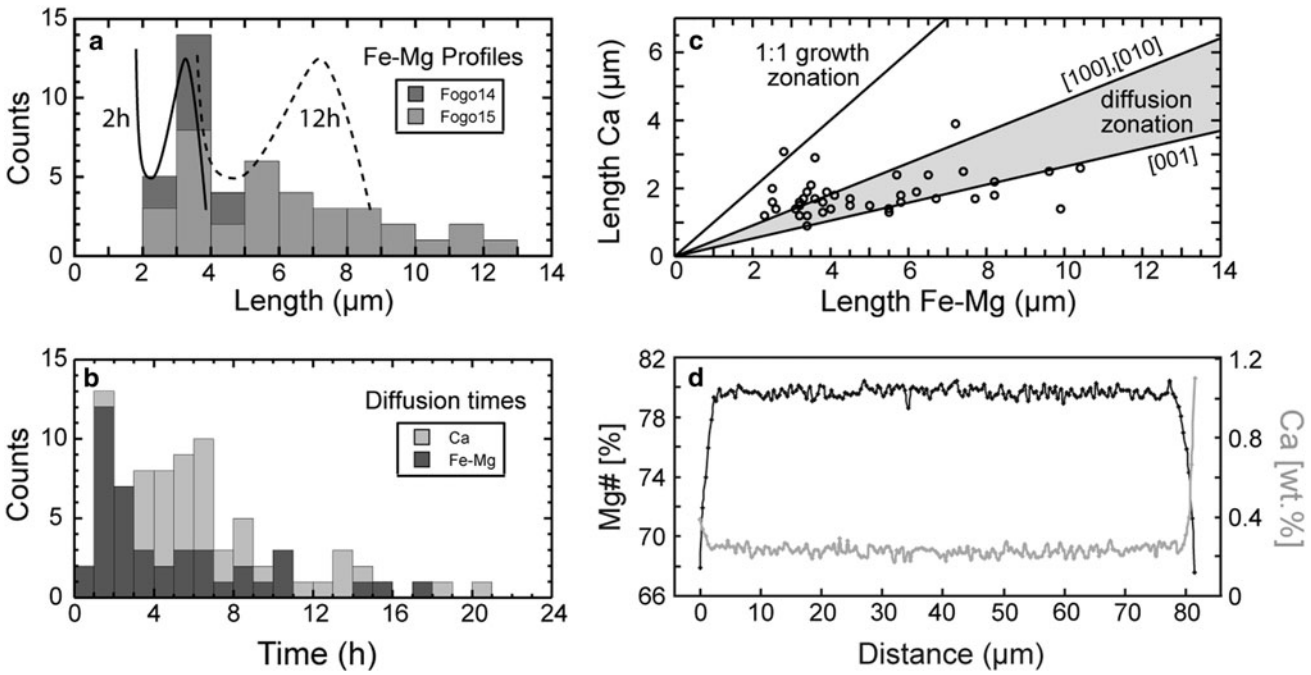

Fig. 10 **a** Calculated lengths for 46 Fo% zonation profiles at the outermost rims of olivine phenocrysts. Curves show distributions of simulated zonation lengths for 5000 randomly oriented crystals at diffusion times of 2 h (*solid*) and 12 h (dashed). **b** Diffusion times calculated for the outermost Fo% and Ca zonations using the diffusion coefficients for the [001] direction as discussed in the text. Average values are 5.9 h for Fo% and 7.8 h for Ca. **c** Comparison of profile lengths of Fo% and Ca zonations. Most data plot in the field for pure diffusional zonation that is limited by two straight lines with slopes of 0.27 and 0.46, i.e., the square root of the D_{Ca}/D_{FeMg} ratios for the different directions. Data outside these limits reflect the effect of crystal growth and uncertainties in the determination of short Ca profile lengths. **d** Example of a zonation profile through an olivine phenocryst (sample Fogo 14_Ol_11)

and 3–7 h for Ca (Fig. 10, Table A6). Remarkably, sample Fogo14 from the main lava flow yields shorter zoning profiles and hence shorter timescales (2.5–4.5 μm and 1.0–3.2 h, respectively; $n = 9$) than sample Fogo15 from the late pahoehoe unit (up to 12.5 μm and 24.7 h; $n = 34$). In addition to actual variations in diffusion times, much of the observed data spread is caused by the following effects not considered in the simple model:

(1) Olivine has a strong diffusion anisotropy: $D^a_{FeMg} \approx D^b_{FeMg} \approx D^c_{FeMg}/6$ and $D^a_{Ca} \approx D^b_{Ca} \approx D^c_{Ca}/2$ (Dohmen and Chakraborty 2007; Coogan et al. 2005). As we consider only the [001] direction in our calculations, the diffusion times derived from Fe–Mg and Ca zonations can be underestimated by a factor of up to 6 and 2, respectively. To assess this effect, we have calculated the distribution of zonation lengths for 5000 random directions by using Eq. (3) for a fixed diffusion time and direction-dependent D_{FeMg} in olivine (e.g. Costa and Chakraborty 2004). The results show that diffusion anisotropy can partly account for variations at zoning profiles <6 μm long (diffusion times of 2–6 h), but cannot explain the observed spread to longer profiles (Fig. 10a). For sample Fogo14, the measured data distribution is almost perfectly simulated by a diffusion time of 3.5 h and random directions.

(2) Geometric artifacts due to two-dimensional sectioning of samples and diffusive flux from the third dimension may result in significant overestimates of the diffusion time (e.g. Pan and Batiza 2002; Costa and Chakraborty 2004). In our study, however, both effects are probably of minor relevance because zoning profiles are short compared to the grain sizes and only olivines with similar core plateau compositions were used for the calculations.

(3) Crystal growth concomitant to diffusion increases the length of zoning profiles and results in overestimates of the diffusion time. The magnitude of this effect may be large due to strong undercooling of the ascending and degassing magma, as is expressed by the large number of microlites in glassy 1995 samples. This effect could explain the tendency for Ca to yield larger diffusion times than Fo% zonations (Fig. 10b), because the weight of crystal growth relative to solid-state diffusion increases with decreasing diffusivities. This is also illustrated by a plot of measured Fo% versus Ca zonation lengths, where short zonations tend to deviate from the diffusion field due to increased Ca lengths (Fig. 10c). In addition, the interpretation that growth dominated over diffusion at short Ca profiles is in accordance with their poor fit by the simple diffusion model.

Despite the effects discussed above and the large scatter for the Ca data, there is a remarkable overlap of diffusion times obtained for Fo% and Ca zonations, but the former yield more robust time constraints. In summary, by considering both anisotropy and crystal growth, our best estimate for actual diffusion times of sample Fogo14 is 1–3 h. For sample Fogo15, the olivine population is more heterogeneous with respect to zoning profiles and we estimate an actual range of diffusion times of 2–12 h. The major factors of uncertainty are believed to be the effect of crystal growth, and the proper choice of the strongly temperature-dependent diffusion coefficients.

Discussion

Interpretation of microthermometric data

Our microthermometric data for CO_2-dominated fluid inclusions in phenocrysts yield important pressure information, but the interpretation of the data set is not straightforward. An analysis of the frequency distributions of fluid densities (Fig. 7b) is necessary to place constraints on the conditions of entrapment and re-equilibration of the studied inclusions.

Re-equilibration can occur when changing ambient conditions lead to differences between inclusion fluid pressure and external pressure or change the host mineral composition. Three main types are distinguished here (reviewed by Bodnar 2003): (a) Volumetric re-equilibration by stretching changes the inclusion volume and occurs by creep mechanisms (Wanamaker and Evans 1989). (b) Re-equilibration by leakage (decrepitation) causes partial or complete loss of fluid. Inclusions showing signs of decrepitation were avoided in our investigations. (c) Compositional re-equilibration causes diffusive loss of components from the trapped fluid (e.g. Bakker and Jansen 1991). This process can explain the virtual absence of H_2O in many CO_2-dominated inclusions. We note that in many cases it is not possible to recognize optically that re-equilibration had occurred. As a general rule, fluid inclusions yield minimum pressure estimates of magma stalling because all re-equilibration processes during magma ascent result in decreasing inclusion densities.

Observation 1: Olivine-hosted fluid inclusions show higher densities—and hence pressures—in phonotephrites (0.67–0.82 g/cm^3, 320–470 MPa; $n = 38$) than in basanites (0.58–0.77 g/cm^3, 270–440 MPa; $n = 181$). This appears counterintuitive because the phonotephrites were erupted before the basanites, and should have ascended from a similar or shallower depth. However, the different densities can be plausibly explained by different rates of

re-equilibration of the inclusions during magma ascent to the surface. Stretching and diffusive loss of H_2O from the trapped fluid must have occurred because both processes occur at high rates that are strongly temperature-dependent. Even if olivine-hosted inclusions in both magma types had the same initial density distribution, a shift to lower densities upon rapid decompression would be larger for the basanites than for the significantly cooler phonotephrites. Because the temperatures for the phonotephrites inferred by clinopyroxene-melt thermometry are well below 1,100°C, the effect of stretching is small if they ascended to the surface in no more than a few hours (Wanamaker and Evans 1989). The limited effect of stretching is also reflected by the overlap of pressures obtained from olivine-hosted inclusions and clinopyroxene-melt barometry of phonotephrites (Fig. 8). With two different petrological approaches yielding similar pressures, this is a robust observation.

Observation 2: Fluid densities are higher in olivine-hosted than in clinopyroxene-hosted inclusions (Fig. 7b) even in the same rock type. This is most intriguing for the phonotephrites, where measured inclusion densities for clinopyroxene (0.51–0.66 g/cm^3, 200–310 MPa; $n = 104$) and olivine (0.67–0.82 g/cm^3, 320–470 MPa) phenocrysts show no overlap. The only plausible explanation for this observation is re-equilibration processes. Apparently, re-equilibration of fluid inclusions during magma ascent occurred faster and/or more complete in clinopyroxene than in olivine, in accordance with previous studies claiming that olivine is the better fluid container (Hansteen et al. 1998; Galipp et al. 2006). Clinopyroxene-hosted fluid inclusions may thus yield better approximations for the pressures of short-term re-equilibration.

Observation 3: The density distributions for clinopyroxene- and olivine-hosted inclusions are well-defined and show a sharp cut-off at 0.51 and 0.67 g/cm^3 (200 and 320 MPa), respectively. They are also not skewed toward lower densities (Fig. 7b), in contrast to observed density distributions of fluid inclusions after gradual decompression and re-equilibration (e.g., Vityk and Bodnar 1998). The implications of this observation are two-fold. First, final magma ascent to the surface must have occurred in a short time (a few hours, see below) so that re-equilibration of inclusions was limited. Second, the data indicate two distinct levels of magma stagnation: a deeper level (400–470 MPa at least) that is mainly reflected by olivine-hosted inclusions, and a shallower level (around 220–300 MPa) where stagnation was long enough for most clinopyroxene-hosted inclusions to re-equilibrate, but not for olivine-hosted ones. Pressures between these levels are believed to reflect incomplete re-equilibration in most cases.

Depths of magma stagnation and fractionation

A distinctive feature of our barometric data is the very little overlap of calculated pressures for fluid inclusions (220–470 MPa) and for clinopyroxene-melt-equilibrium (460–680 MPa; Fig. 8). A similar tendency to lower pressures of fluid inclusion data has been recognized in previous studies at different localities (Hansteen et al. 1998; Nikogosioan et al. 2002; Schwarz et al. 2004; Galipp et al. 2006).

There are some possible causes for the distinct pressure ranges obtained by both barometric methods. (1) The model temperature used to obtain pressures from calculated isochores may be inappropriate. This is rather unlikely; because of the isochores' little $\Delta P/\Delta T$, the model temperatures would have to be unreasonably high (e.g., 1,150°C for the phonotephrite) for a complete overlap with the clinopyroxene-melt equilibrium data. (2) The barometer of Putirka et al. (2003) may yield inaccurate pressures for highly alkalic Si-undersaturated melts. This effect appears to be limited because of the wide range of melt compositions used for calibration and because calculated pressures for alkalic magmas are consistent with other barometric data (cf. Klügel et al. 2005). The systematic error of our calculated pressures is believed to be within 130 MPa (derived for a test data set; Putirka et al. 2003). (3) Compared to clinopyroxene-melt equilibria, fluid inclusions respond much faster, and by different mechanisms, to decompression during magma ascent. Volumetric or compositional re-equilibration of fluid inclusions at magmatic temperatures can occur during hours to days (summarized in Bodnar 2003; Hansteen and Klügel 2008), which is too short to be recorded by clinopyroxene equilibrating with a melt. For example, the growth of a 5–10 μm wide clinopyroxene rim at near-equilibrium conditions, or the diffusive re-equilibration along 5–10 μm (the distance used for the microprobe measurements), would require several months (Putirka 1997; Cashman 1990).

Taking together these considerations and the pressure distributions shown in Fig. 8, a consistent scenario arises. We interpret the pressure range of 460–680 MPa obtained by clinopyroxene-melt-thermobarometry as upper and lower bounds for the level where clinopyroxene and olivine phenocrysts crystallized before eruption, probably in a small magma reservoir. Corresponding depths are ~16–24 km, in the uppermost mantle just below the Moho (12–14 km depth; Pim et al. 2008; Lodge and Helffrich 2006). The weak tendency of the phonotephrites for lower pressures may reflect slightly shallower storage depth, or a bias due to the evolved melt composition, or the small number of data points. The pressures indicated by olivine-hosted fluid inclusions in phonotephrites (400–470 MPa) are fully consistent with the clinopyroxene-melt data when

considering that some re-equilibration of inclusions must have occurred. A mere correction for a complete loss of e.g. 10 mol% of H_2O from the inclusions would shift the range to 400–620 MPa (cf. Hansteen and Klügel 2008).

The fluid inclusion data indicate the existence of a shallower level (around 220–310 MPa, 8–11 km depth) where the ascending magmas briefly stagnated before reaching the surface. Stagnation periods were probably on the order of a few hours to days, too short to be reflected by clinopyroxene barometry but long enough for re-equilibration of fluid inclusions in clinopyroxene phenocrysts and, to a lesser degree, in olivine. This depth range is probably within the lower, intrusive oceanic crust (Pim et al. 2008); it may be closer to the Moho depth than indicated by the data if effects of re-equilibration are accounted for. The cause for ascending magmas to stagnate at this level is probably related to the density change at the Moho. We note that a similar depth range for magma ponding is inferred for the active Cumbre Vieja volcano on La Palma (Canary Islands), where it is supported by the common occurrence of gabbro xenoliths from the lower crust (Klügel et al. 2005).

The third maximum around 340–460 MPa displayed in Fig. 8 is not interpreted as another stagnation level for ascending magmas, as this would require too much special pleading. This pressure range rather reflects the effect of incomplete re-equilibration of olivine-hosted inclusions as discussed above, although the former interpretation cannot be ruled out completely.

It should be emphasized here that our data do not provide any evidence for shallow magma storage in the crust or within the volcanic edifice. Our clinopyroxene-melt barometry data support the inference by Amelung and Day (2002), based on InSAR data and a simple deformation model, that the 1995 magma chamber was located at >16.5 km depth. They also overlap partly with the rather large pressure range of 22–42 km estimated by Munhá et al. (1997) for wehrlite xenoliths. In contrast, the depth of origin of pyroxenite xenoliths obtained by these authors is significantly shallower (13 ± 3 km). This difference may indicate that the pyroxenites were not cognate to the 1995 eruption but represent cumulates from older magma batches that were picked up by the 1995 magmas. We note that this scenario is supported by our implication for a short-term stagnation level in the lower crust where remaining magma batches would ultimately form cumulates.

Constraints on magma ascent rates

The observed rim zonations of olivine phenocrysts are interpreted to reflect a short-term disequilibrium with the ascending host melt caused by rapid decompression, degassing and crystal growth. Our best estimate for the duration of this disequilibrium is around 1–3 h for sample Fogo14 and 2–12 h for Fogo15 (Fig. 10), which allows placing constraints on the ascent velocity of the magma. It is not known, however, at which depth the degassing-induced crystal growth initiated the diffusion clock. The fluid inclusions indicate that the magma was vapor-saturated at >440 MPa, thus an ascent from these depths inevitably causes degassing. During progressive depressurisation, degassing–and hence undercooling of the melt–strongly increases at <200 MPa due to the non-linear dependence of H_2O solubility on pressure (Dixon 1997).

We conclude that most of the olivine zonations formed during the final ascent from the stalling level in the lower crust (220 MPa or 8 km depth). In this case, the average magma ascent rate would be on the order of 0.7–2.2 m/s for sample Fogo14 and 0.2–1.1 m/s for Fogo15. These are minimum values because diffusion had continued in the cooling lava flows for some time after eruption, and because the effect of crystal growth on the zoning profiles may have been underestimated. Interestingly, the sample from the main lava flow yields faster ascent rates than the sample from the late pahoehoe flow, which is consistent with decreasing activity toward the end of the eruption (Réffega et al. 1997).

Alternatively, if the diffusion clock were initiated when the magma began to ascend from the inferred reservoir in the mantle, the average ascent rates indicated by sample Fogo14 would range from 1.5–4.4 m/s (beginning at 16 km depth) to 2.2–6.7 m/s (beginning at 24 km). The duration of magma stagnation in the lower crust and re-equilibration of fluid inclusions would be limited to 1–3 h, and peak ascent rates would be higher. Altogether we render this scenario as less likely.

Differentiation of the 1995 magmas

Even the most primitive basanites of the 1995 eruption are relatively differentiated with Ni contents of ≤65 ppm and MgO <7 wt%, which requires considerable olivine and clinopyroxene fractionation in mantle reservoirs. Although the basanites are inferred to be cogenetic with the earlier erupted phonotephrites, both are unlikely to have co-existed in a single zoned magma reservoir for a long period of time. Assuming H_2O contents of 1 wt% in both magma types and temperatures of 1,100°C and 1,030°C, respectively, calculated viscosities range from 90 to 120 Pa s for the basanites and 1,670–2,590 Pa s for phonotephrites (Hui and Zhang 2007). Had the melts co-existed in a stratified magma chamber, these low viscosities and the large temperature difference would certainly have resulted in significant mixing and not in a bimodal suit of erupted magmas as observed. We thus envisage a geometrically

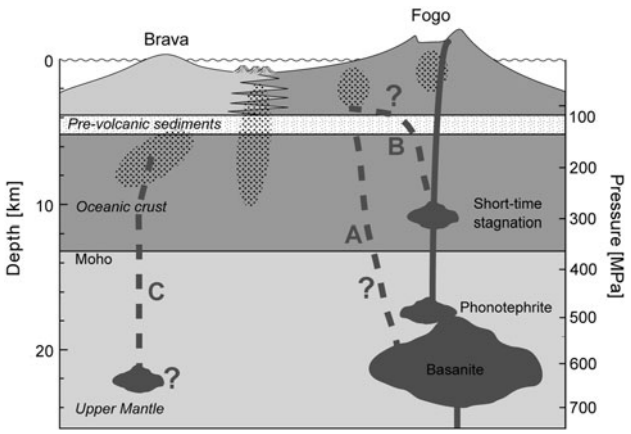

Fig. 11 Schematic model of the magma plumbing system of the 1995 Fogo eruption (thicknesses of crustal layers after Pim et al. (2008)). Fractional crystallization prior to eruption took place between 16 and 24 km depth in the uppermost lithospheric mantle. Early erupted phonotephrites are cogenetic with the subsequently erupted basanites and are interpreted to have evolved in a small pocket with limited connection to the main magma chamber. The ascending magma stalled briefly in the lower crust. *Dotted areas mark* the positions of hypocenters during the small seismic crisis of 1994 (Heleno da Silva et al. 1997; Heleno and Fonseca 1999), which may have been caused by propagating dikes preceding the 1995 eruption (dikes A and B) and/or by dikes related to a plumbing system beneath Brava (C)

complex magma reservoir for the 1995 eruption with a small magma pocket having limited connection to the main chamber (Fig. 11). Such a geometry could result in a higher cooling rate of the small pocket resulted in a higher grade of crystal fractionation and formation of phonotephrite and could inhibit convective mixing of the different melts. The magma ascent preceding the eruption started with the phonotephrite in the partially separated pocket and continued with the major magma batch of basanitic to tephritic composition. This model is consistent with the chemical and mineralogical zonation of the erupted lavas, with the little mixing of both melt types observed, and with similar pressure ranges for both magmas indicated by clinopyroxene-melt equilibria.

Is there a deep connection between Fogo and Brava?

The suggestion of a possible relation of the 1995 eruption to the magma plumbing system of Brava (Heleno 2003) was based on the unusual orientation of eruptive fissures, the unusual occurrence of evolved lavas, and the observed seismicity between both islands in 1994. This scenario, which would involve lateral magma movement at probably 2–7 km depth beneath the Fogo-Brava platform, is not supported by our combined petrological, geochemical, and isotopic data. First, if lateral flow of magma had occurred at 2–7 km depth (~50–180 MPa) over considerable distances, this pressure should be reflected in some of the investigated fluid inclusions at least. Not a single inclusion, however, indicated a pressure less than 200 MPa despite careful study. Second, the major and trace element data indicate derivation of the 1995 phonotephrites from the basanites and rule out significant involvement of Brava material. Third, the isotopic fingerprints of recent Brava phonolites and basanites differ significantly from those of the 1995 Fogo eruption and other historic and prehistoric Fogo samples (Fig. 5) which indicates distinct regions of partial melting in the mantle for both islands.

We thus conclude that magma ascent of the 1995 eruption occurred along the established magma plumbing system beneath Fogo without any interaction with the magma feeding system of Brava (Fig. 11). The evolved character of the zoned eruption appears to be fortuitous. Although our data suggest that short-term stagnation of ascending magma had occurred within the lower crust, possibly combined with some lateral movement, subhorizontal magma transport within the upper crust over larger distances can be ruled out. The SW-orientation of the 1995 eruptive fissures toward Brava merely reflects the local stress field near the surface. The feeder dike was found to be a planar, steeply NW-dipping sheet with a strike of ~60° that extended to a depth of 4 km at least (Heleno da Silva et al. 1999); there have been no indicators for lateral dike propagation from the SW prior to eruption. The seismic crisis below Brava and between the two islands in early 1994 was probably caused by one or more propagating dikes that did not reach the surface; possible interpretations are marked in Fig. 11. Hypothetical dikes A and B are related to the magma batch that later fed the 1995 eruption, C is fed by a hypothetical reservoir below Brava and is independent from Fogo magmatism. The seismicity between Fogo and Brava was probably related to the morphologically young volcanic cones in this area (Le Bas et al. 2007), but so far nothing is known about the respective source.

Conclusions

1. Geochemical data and modeling of crystal fractionation shows that basanites and phonotephrites of the bimodal 1995 Fogo eruption are cogenetic. Differentiation of phonotephrites probably occurred in a smaller magma pocket with limited connection to the main magma chamber.
2. Clinopyroxene-melt barometry and fluid inclusion data provide insight into the magma plumbing system of the 1995 eruption. Before eruption the magma was stored within 460–680 MPa, corresponding to 16–24 km depth, in the uppermost mantle. During the eruption, the ascending magma stagnated for a short time at 220–310 MPa (8–11 km depth).

3. During the eruption the magma passed through the crust within less than 12 h, probably 1–4 h. Stagnation in the lower crust was restricted to periods of a few hours. Our data provide no evidence for prolonged magma storage at shallow levels (<200 MPa) or lateral magma movements within the Fogo-Brava platform.
4. Pre-eruptive seismicity on Brava and below the channel between Fogo and Brava in 1994 was probably caused by a propagating dike, which may have been related to the later 1995 eruption, or to a group of active submarine volcanoes in the channel.
5. Magma ascent of the 1995 eruption occurred along the established magma plumbing system of Fogo without interaction with the plumbing system near Brava. A seismic crisis in the channel between Brava and Fogo does not necessarily herald a new eruption on Fogo.

Acknowledgments Our field work on Fogo would not have been possible without the support by Simon Day, Bruno Faria, José Antonio, and the Cape Verde Ministério do Ambiente e Agricultura/ Parque Natural do Fogo. We thank Thor Hansteen, Sandra Heleno da Silva, Thomas Kokfelt, Ricardo Ramalho and Simon Day for stimulating discussions and help, and Mario Thöner and Heike Anders for analytical support. This study was supported by the Deutsche Forschungsgemeinschaft (DFG grants KL1313/9 and HA2100/12).

References

Amelung F, Day S (2002) InSAR observations of the 1995 Fogo, Cape Verde, eruption: implications for the effects of collapse events upon island volcanoes. Geophys Res Lett 29(12):GL013760

Andersen T, Neumann E (2001) Fluid inclusions in mantle xenoliths. Lithos 55:301–320

Angus S, Armstrong B, de Reuck K, Altunin V, Gadetskii O, Chapela G, Rowlinson J (1976) International tables of fluid state, carbon dioxide, vol 3. Pergamon Press, Oxford, pp 1–385

Bakker R, Jansen J (1991) Experimental post-entrapment water loss from synthetic CO2–H2O inclusions in natural quartz. Geochim Cosmochim Acta 55:2215–2230

Barker AK, Holm PM, Peate DW, Baker JA (2009) Geochemical stratigraphy of submarine lavas (3–5 Ma) from the Flamengos Valley, Santiago, Southern Cape Verde Islands. J Petrol 50(1):169–193

Bodnar RJ (2003) Re-equilibration of fluid inclusions. In: Samson I, Anderson A, Marshall D (eds) Fluid inclusions: analysis and interpretation. Mineral Assoc Can, Short Course Ser 32:213–230

Bottinga Y, Richet P (1981) High pressure and temperature equation of state and calculation of the thermodynamic properties of gaseous carbon dioxide. Am J Sci 281(5):615–660

Brum da Silveira A, Madeira J, Serralheiro A, Torres P, Silva L, Mendes M (1997) O controlo estrutural da erupção de abril de 1995 na Ilha do Fogo, Cabo Verde. In: Réffega A et al (eds) A Erupção Vulcanica de 1995 na Ilha do Fogo, Cabo Verde. Ministério da Ciencia e da Tecnologia; Instituto de Investigação Científica Tropical, Lisbon, pp 51–61

Cashman KV (1990) Textural constraints on the kinetics of crystallization of igneous rocks. In: Nicholls J, Russell JK (eds) Modern methods of igneous petrology: understanding magmatic processes. Rev Mineral 24:259–314

Chatterjee N, Bhattacharji S, Fein C (2005) Depth of alkalic magma reservoirs below Kolekole cinder cone, Southwest rift zone, East Maui, Hawaii. J Volcanol Geotherm Res 145:1–22

Coogan L, Hain A, Stahl S, Chakraborty S (2005) Experimental determination of the diffusion coefficient for calcium in olivine between 900°C and 1500°C. Geochim Cosmochim Acta 69(14):3683–3694

Correia E, Costa F (1995) Breve notícia da recente erupção na Ilha do Fogo e suas consequências. Finisterra XXX(59–60):165–175

Costa F, Chakraborty S (2004) Decadal time gaps between mafic intrusion and silicic eruption obtained from chemical zoning patterns in olivine. Earth Planet Sci Lett 227(3–4):517–530

Crank J (1975) The mathematics of diffusion. Oxford University Press, London, pp 1–414

Day SJ, Heleno da Silva S, Fonseca J (1999) A past giant lateral collapse and present-day flank instability of Fogo, Cape Verde Islands. J Volcanol Geotherm Res 94:191–218

Dixon JE (1997) Degassing of alkalic basalts. Am Mineral 82:368–378

Dohmen R, Chakraborty S (2007) Fe-Mg diffusion in olivine II: point defect chemistry, change of diffusion mechanisms and a model for calculation of diffusion coefficients in natural olivine. Phys Chem Miner 34:409–430

Doucelance R, Escrig S, Moreira M, Gariepy C, Kurz M (2003) Pb-Sr-He isotope and trace element geochemistry of the Cape Verde Archipelago. Geochim Cosmochim Acta 67(19):3717–3733

Duggen S, Hoernle KA, Hauff F, Klügel A, Bouabdellah M, Thirlwall M (2009) Flow of Canary mantle plume material through a subcontinental lithospheric corridor beneath Africa to the Mediterranean. Geology 37:283–286

Duke J (1976) Distribution of the period four transition elements among olivine, calcic clinopyroxene and mafic silicate liquid: experimental results. J Petrol 17(4):499–521

Escrig S, Doucelance R, Moreira M, Allègre C (2005) Os isotope systematics in Fogo Island: evidence for lower continental crust fragments under the Cape Verde Southern Islands. Chem Geol 219:93–113

Foeken J, Day S, Stuart F (2009) Cosmogenic ^{3}He exposure dating of the Quaternary basalts from Fogo, Cape Verdes: implications for rift zone and magmatic reorganisation. Quat Geochronol 4:37–49

Frezzotti M, Andersen T, Neumann E, Simonsen S (2002) Carbonatite melt-CO_2 fluid inclusions in mantle xenoliths from Tenerife, Canary Islands: a story of trapping, immiscibility and fluid-rock interaction in the upper mantle. Lithos 64:77–96

Galipp K, Klügel A, Hansteen TH (2006) Changing depths of magma fractionation and stagnation during the evolution of an oceanic island volcano: La Palma (Canary Islands). J Volcanol Geotherm Res 155(3–4):285–306

Garcia MO, Ho RA, Rhodes JM, Wolfe EW (1989) Petrologic constraints on rift-zone processes; results from episode 1 of the Puu Oo eruption of Kilauea Volcano, Hawaii. Bull Volcanol 52(2):81–96

Geist D, White W, Naumann T, Reynolds R (1999) Illegitimate magmas of the Galápagos: insights into mantle mixing and magma transport. Geology 27(12):1103–1106

Grevemeyer I, Helffrich G, Faria B, Booth-Rea G, Schnabel M, Weinrebe W (2010) Seismic activity at Cadamosto seamount near Fogo Island, Cape Verdes–formation of a new ocean island? Geophys J Int 180:552–558

Hansteen TH, Klügel A (2008) Fluid inclusion thermobarometry as a tracer for magmatic processes. In: Putirka K, Tepley III F (eds) Minerals, inclusions and volcanic processes. Rev Mineral 69:142–177

Hansteen TH, Klügel A, Schmincke H-U (1998) Multi-stage magma ascent beneath the Canary Islands: evidence from fluid inclusions. Contrib Mineral Petrol 132:48–64

Hart SR (1984) A large-scale isotopic anomaly in the southern hemisphere mantle. Nature 309:753–757

Heleno S (2003) O Vulcão do Fogo–Estudo Sismológico. Ph.D. thesis, Instituto Português de Apoio ao Desenvolvimento, Lisbon, pp 1–464

Heleno da Silva S, Foulger G, Barros I, Querido A, Walker A, Fonseca J (1997) Seismic activity in Fogo and Brava Islands, Cape Verde. In: Réffega A et al (eds) A Erupção Vulcânica de 1995 na Ilha do Fogo, Cabo Verde. Ministério da Ciencia e da Tecnologia; Instituto de Investigação Científica Tropical, Lisbon, pp 79–81

Heleno da Silva S, Day SJ, Fonseca J (1999) Fogo Volcano, Cape Verde Islands: seismicity-derived constraints on the mechanism of the 1995 eruption. J Volcanol Geotherm Res 94:219–231

Heleno SIN, Fonseca JFBD (1999) A seismological investigation of the Fogo Volcano, Cape Verde Islands: preliminary results. Volc Seis 20:199–217

Helffrich G, Heleno SIN, Faria B, Fonseca JFBD (2006) Hydroacoustic detection of volcanic ocean-island earthquakes. Geophys J Int 167:1529–1536

Hoernle K, Abt DL, Fischer KM, Nichols H, Hauff F, Abers GA, van den Bogaard P, Heydolph K, Alvarado G, Protti M, Strauch W (2008) Arc-parallel flow in the mantle wedge beneath Costa Rica and Nicaragua. Nature 451:1094–1097

Hoernle K, Hauff F, Kokfelt TF, Haase K, Garbe-Schönberg D, Werner R (2011) On- and off-axis chemical heterogeneities along the South Atlantic Mid-Ocean-Ridge (5-11°S): shallow or deep recycling of ocean crust and/or intraplate volcanism? Earth Planet Sci Lett (accepted with minor revisions)

Hollister L (1990) Enrichment of CO_2 in fluid inclusions in quartz by removal of H_2O during crystal-plastic deformation. J Struct Geol 12(7):895–901

Holloway JR (1981) Volatile interactions in magmas. In: Newton R, Navrotsky A, Wood B (eds) Thermodynamics of minerals and melts. Springer, New York, pp 273–293

Holm PM, Grandvuinet T, Friis J, Wilson R, Barker AK, Plesner S (2008) An 40Ar-39Ar study of the Cape Verde hot spot: temporal evolution in a semistationary plate environment. J Geophys Res 113:B08201. doi:08210.01029/02007JB005339

Hui H, Zhang Y (2007) Toward a general viscosity equation for natural anhydrous and hydrous silicate melts. Geochim Cosmochim Acta 71(2):403–416

Kerrick DM, Jacobs GK (1981) A modified Redlich-Kwong Equation for H_2O, CO_2, and H_2O-CO_2 mixtures at elevated pressures and temperatures. Am J Sci 281(6):735–767

Klügel A, Hoernle KA, Schmincke HU, White JDL (2000) The chemically zoned 1949 eruption on La Palma (Canary Islands): Petrologic evolution and magma supply dynamics of a rift-zone eruption. J Geophys Res 105(B3):5997–6016

Klügel A, Hansteen TH, Galipp K (2005) Magma storage and underplating beneath Cumbre Vieja volcano, La Palma (Canary Islands). Earth Planet Sci Lett 236:211–226

Kokfelt T (1998) A geochemical and isotopic study of the Island of Fogo, the Cape Verde Islands. PhD thesis. University of Copenhagen, pp 164

Kress V, Carmichael I (1991) The compressibility of silicate liquids containing Fe_2O_3 and the effect of composition, temperature, oxygen fugacity and pressure on their redox state. Contrib Mineral Petrol 108:82–92

Le Bas T, Masson D, Holtom R, Grevemeyer I (2007) Slope failures of the flanks of the southern Cape Verde Islands. In: Lykousis V, Sakellariou D, Locat J (eds) Submarine mass movements and their consequences. Springer, Berlin, pp 337–345

Lodge A, Helffrich G (2006) Depleted swell root beneath the Cape Verde Islands. Geology 34:449–452

Mackwell SJ, Kohlstedt DL (1990) Diffusion of Hydrogen in olivine–implications for water in the mantle. J Geophys Res Solid 95(B4):5079–5088

Madeira J, Mata J, Mourão C, Brum da Silveira A, Martins S, Ramalho R, Hoffmann DL (2010) Volcano-stratigraphic and structural evolution of Brava Island (Cape Verde) based on 40Ar/39Ar, U-Th and field constraints. J Volcanol Geothermal Res 196(3–4):219–235

Munhá J, Mendes M, Palácios T, Silva L, Torres P (1997) Petrologia e Geoquímica da Erupção de 1995 e de Outras Lavas Históricas na Ilha do Fogo, Cabo Verde. In: Réffega A et al (eds) A Erupção Vulcânica de 1995 na Ilha do Fogo. Cabo Verde. Ministério da Ciencia e da Tecnologia, Instituto de Investigação Científica Tropical, Lisbon, pp 171–186

Nikogosioan I, Elliott T, Touret J (2002) Melt evolution beneath thick lithosphere: a magmatic inclusion study of La Palma, Canary Islands. Chem Geol 183:169–193

Pan Y, Batiza R (2002) Mid-ocean ridge magma chamber processes: constraints from olivine zonation in lavas from the East Pacific Rise at 9°30'N and 10°30'N, J Geophys Res 107: 10.1029/2001JB000435

Peccerillo A, Frezzotti ML, De Astis G, Ventura G (2006) Modeling the magma plumbing system of Vulcano (Aeolian Islands, Italy) by integrated fluid-inclusion geobarometry, petrology, and geophysics. Geology 34:17–20

Pim J, Peirce C, Watts A, Grevemeyer I, Krabbenhoeft A (2008) Crustal structure and origin of the Cape Verde Rise. Earth Planet Sci Lett 272:422–428

Putirka K (1997) Magma transport at Hawaii: inferences based on igneous thermobarometry. Geology 25(1):69–72

Putirka K (1999) Clinopyroxene + liquid equilibria to 100 kbar and 2450 K. Contrib Mineral Petrol 135:151–163

Putirka K, Mikaelian H, Ryerson F, Shaw H (2003) New clinopyroxene-liquid thermobarometers for mafic, evilved, and volatile-bearing lava compositions, with applications to lavas from Tibet and the Snake River Plain, Idaho. Am Mineral 88:1542–1554

Réffega A, Figueiredo M, Silva L, Costa F, Mendes M, Torres P, da Silva T, Correia E (1997) A Erupção Vulcânica de 1995 na Ilha do Fogo. Cabo Verde. Ministério da Ciencia e da Tecnologia, Instituto de Investigação Científica Tropical, Lisbon, p 422

Rhodes JM, Wenz KP, Neal CA, Sparks JW, Lockwood JP (1989) Geochemical evidence for invasion of Kilauea's plumbing system by Mauna Loa magma. Nature 337(6204):257–260

Roedder E (1984) Fluid inclusions. Rev Mineral 12:644

Schwarz S, Klügel A, Wohlgemuth-Ueberwasser C (2004) Melt extraction pathways and stagnation depths beneath the Madeira and Desertas rift zones (NE Atlantic) inferred from barometric studies. Contrib Mineral Petrol 147:228–240

Silva L, Mendes M, Torres P, Palácios T, Munhá J (1997) Petrografia e Mineralogia das Formaçoe Vulcanicas da Erupção da 1995 na Ilha do Fogo, Cabo Verde. In: Réffega A et al (eds) A Erupção Vulcânica de 1995 na Ilha do Fogo, Cabo Verde. Ministério da Ciencia e da Tecnologia, Instituto de Investigação Científica Tropical, Lisbon, pp 165–170

Span R, Wagner W (1996) A new equation of state for Carbon dioxide covering the fluid region from the Triple-point temperature to 1100 K at pressures up to 800 MPa. J Phys Chem Ref Data 25(6):1509–1596

Sparks R, Pinkerton H (1978) Effect of degassing on rheology of basaltic lava. Nature 276(23):385–386

Sterner S, Pitzer K (1994) An equation of state for carbon dioxide valid from zero to extreme pressures. Contrib Mineral Petrol 117:362–374

Stroncik NA, Klügel A, Hansteen TH (2009) The magmatic plumbing system beneath El Hierro (Canary Islands): constraints from phenocrysts and naturally quenched basaltic glasses in submarine rocks. Contrib Mineral Petrol 157:593–607

Sun S-s, McDonough W (1989) Chemical and isotopic systematics of oceanic basalts: implications for mantle composition and processes. In: Saunders A, Norry M (eds) Magmatism in the Ocean Basins, Geological Society, London, Special Publications 42:313–345

Torres P, Madeira J, Silva L, Brum da Silveira A, Serralheiro A, Mota Gomes A (1997) Carta Geológica das erupções históricas da Ilha do Fogo: Revisão e actualização. In: Réffega A, Figueiredo M, Silva L, Costa F, Mendes M, Torres P, da Silva T, Correia E (eds) A Erupção Vulcânica de 1995 na Ilha do Fogo, Cabo Verde. Ministério da Ciencia e da Tecnologia, Instituto de Investigação Científica Tropical, Lisbon, pp 119–132

van den Kerkhof A (1990) Isochoric phase diagrams in the systems CO2-CH4 and CO2–N2: Application to fluid inclusions. Geochim Cosmochim Acta 54:621–629

Vityk MO, Bodnar RJ (1998) Statistical microthermometry of synthetic fluid inclusions in quartz during decompression reequilibration. Contrib Mineral Petrol 132(2):149–162

Wanamaker B, Evans B (1989) Mechanical re-equilibration of fluid inclusions in San Carlos olivine by power-law creep. Contrib Mineral Petrol 102:102–111

Wolff J, Turbeville B (1985) Recent pyroclastic deposits on Brava, Cape Verde Islands. (abs). Eos, Trans Amer Geophys Union 66(46):1152